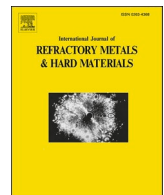




Contents lists available at ScienceDirect

# International Journal of Refractory Metals and Hard Materials

journal homepage: [www.elsevier.com/locate/IJRMHM](http://www.elsevier.com/locate/IJRMHM)



## Wear detection of WC-Cu based impregnated diamond bit matrix based on SEM image and deep learning

Wucheng Sun <sup>a</sup>, Hui Gao <sup>a,b</sup>, Songcheng Tan <sup>a,b,\*</sup>, Zhiming Wang <sup>a</sup>, Longchen Duan <sup>a,b,\*</sup>

<sup>a</sup> Faculty of Engineering, China University of Geosciences, Wuhan 430074, China

<sup>b</sup> International Joint Research Center for Deep Earth Drilling and Resource Development, Wuhan 430074, China



### ARTICLE INFO

#### Keywords:

Metal matrix composite

Wear detection

Scanning electron microscope image

Mask R-CNN

### ABSTRACT

The working efficiency and lifetime of impregnated diamond tools are closely related to their wear conditions, among which different wear modes of the metal matrix play an essential role. Since traditional qualitative description cannot meet the requirement of mathematical relationship establishment, a deep learning method, Mask R-CNN, was applied for the quantitative determination of the matrix wear based on scanning electron microscope (SEM) images. A series of WC-Cu based metal matrix composite (MMC) samples had been prepared by hot-pressed sintering, followed by a pin-on-disc wear test to obtain the wear surface images, and the datasets were established based on a normal wear classification principle where classification is of four basic types: abrasive wear, adhesive wear, fatigue wear and corrosion wear (corrosion wear is not involved in this study). After training, validation, and test based on the SEM wear image datasets, the wear segmentation results from the trained model indicated that Mask R-CNN could automatically identify the wear of metal matrices efficiently and accurately, which was in good agreement with the results obtained by manual labelling. By modifying the algorithm codes, the masks of abrasive, adhesive, and fatigue wear were extracted and counted for model effectiveness evaluation. Moreover, the wear condition values (i.e., wear region areas) obtained from extracted masks would be easily applied for correlation analysis between cutting tool qualities and drilling efficiencies in future research as well. In comparison with statistic results by artificial cognition, the three types of wear showed an average wear region mask IoU over 70%, and an average wear region area loss of less than 3%. In the process of wear detection on similar wear images in published work, the Mask R-CNN model also presented good performances. All related codes and SEM image datasets are available at [https://github.com/sunwucheng/IDB\\_matrix\\_wear](https://github.com/sunwucheng/IDB_matrix_wear).

### 1. Introduction

With ongoing worldwide exploring target converting to deep mineral deposits [1,2] and geothermal resources [3], the demand for deep hard rock drilling has risen sharply in recent years. Impregnated diamond bit (IDB), containing a working layer of diamond reinforced metal matrix composite, has been proven to be an efficient cutting tool against dense and hard rocks [4]. Apart from application in energy exploration, there are also impregnated diamond tools utilized in many other fields, such as construction [5], stone, and civil engineering [6] industry, where the wears of MMCs are all much concerned. For deep hard rock drilling, the rotary drilling bits would suffer from various wear damages, which may result in premature failure and even destruction of the whole set of drilling tools [7]. In exertion of the diamond bit, what plays the key role

is the thrust along with the spin of synthetic diamond grits embedded in the IDB matrix. The composite matrices are expected to be worn synchronously with diamond edges to ensure the best drilling performance, involving penetration efficiency and service life. Hence there have launched multiple studies on the diamond impregnated bits [8–12], including research on diamonds [13], metal matrices [14], and the wear mechanisms [15]. Considering that the service life and working performance of diamond tools are largely determined by metal matrices for the diamond retention capacity [16], it is of great importance to pay close attention to the analysis of the wear mechanism of metal matrices. This study focuses on the quantitative evaluation of metal matrix wear in an accurate and efficient way.

Wear identification and detection have been in research for a long time [17]. Many technologies and methods have been applied for wear

\* Corresponding authors at: No. 388 Lumo Road, Wuhan, Hubei, PR China.

E-mail addresses: [wstansongcheng@cug.edu.cn](mailto:wstansongcheng@cug.edu.cn) (S. Tan), [duanlongchen@163.com](mailto:duanlongchen@163.com) (L. Duan).

measurements of impregnated diamond bits, like optical profilometry [18], fractal theory [19], and statistical analysis [20]. However, correlation analyses may not meet the need for straightforward evaluation of the wear condition. To our knowledge, one of the most common means is to carry out a pin-on-disc wear test and to obtain the wear surface of test samples for SEM analysis. To be specific, the wear mode of MMCs could be described as a combination of several wear types characterized by some specific morphologies on SEM images. For instance, plow grooves due to scratching indicate abrasive wear, and smear implies adhesive wear [21]. However, qualitative description of the worn surface morphologies, illustrating the existence of some wear types and comparing the degrees of wear among different samples, is only on a primary stage. Moreover, with widely differing perspectives, the final results and conclusions are likely to vary from person to person, especially after the increase of the sample size.

A potential method is the convolutional neural network (CNN), which has exhibited excellent performance in automatic detection. For wear mechanism assessment, there was research proposing a two-level inference system made up of one wear mechanism CNN and three wear severity CNN for automated assessment of gear wear mechanism and severity [22]; and in a more common application, the deep learning model of CNN was used for wear debris classification, indicating the wear condition in an indirect manner [23]; Besides, in the form of amplitude-time evolutional curves, the acoustic emission signals in rock drilling [24,25] have the potential to be processed and analyzed with neural network method as well. As one of the most effective CNNs, Mask R-CNN is a very suitable method for instance segmentation to handle the issues in wear detection and evaluation. Since proposed in 2017 [26], Mask R-CNN has been widely used in many fields, such as concrete assessment [27,28], material detection [29,30], precision agriculture [31,32] and medical image [33,34]. In this work, Mask R-CNN was used for wear detection on SEM images, which had been proved feasible in other applications [35,36]. By changing proportions of the main components, WC and Cu, a series of WC-Cu based matrix samples in the shape of cuboid were manufactured by powder metallurgy and hot-pressed sintering for the requirement of wear image datasets first. Then the end faces of the prepared samples were worn against grinding wheels perpendicularly in a pin-on-disc test, and finally got captured by a scanning electron microscope. In this study, the wear mode on an image was described as a combination of different degrees of abrasive, adhesive, and fatigue wear (corrosion wear was exclusive in this research). By manual labeling of the wear regions, the obtained SEM images were divided into the training set, validation set, and test set for the establishment of the Mask R-CNN model. After the Mask R-CNN model was obtained, 100 images in the datasets would be selected for calculation of mask IoU, area loss, and some other wear indexes to make the effectiveness evaluation. Besides, wear images in previous research were added into the test set for verification of its detection effect. The whole computational process was conducted online with Google Colab (online development environment) and Detection2 (software system to implement Mask R-CNN) [37], which means all steps can be repeated easily.

## 2. Materials and methods

### 2.1. Wear image preparation

To obtain the wear images of metal matrices, a series of WC-Cu based powder combinations were determined based on previous experience [38], whereafter powder metallurgy and hot-pressing methods were applied for manufacturing of the MMC samples. All involved powder mixtures and their physical properties in this work are listed below in Table 1.

The metal powders could be divided into three types from their existing states during the process of hot pressing, i.e., skeleton components with the highest melting temperature remaining pure solid phase

**Table 1**

Involved metal powders and their physical properties.

Metal power	WC	663-Cu*	Ni	Co	Mn
Density (g/cm <sup>3</sup> )	15.63	8.82	8.90	8.70	7.43
Melting temperature (°C)	2785	900	1455	1495	1246
Average size (μm)	4	75	45	2	75

\* 663-Cu is a kind of pre-alloyed powder with a composition of Cu<sub>85</sub>Sn<sub>6</sub>Zn<sub>6</sub>Pb<sub>3</sub> (wt%).

to maintain the overall hardness and abrasiveness of the sintered matrix composite (e.g., WC in this work), intermediate components with moderate melting temperatures presenting molten phase to adjust strength and toughness of the matrix (e.g., Ni, Co, Mn in this work), and bonding components with the lowest melting temperatures as the liquid phase to bond other all materials within the matrix (e.g., 663-Cu in this work). According to this, by changing the ratio of the skeleton component (i.e., WC) to the bonding component (i.e., 663-Cu) while volume fractions of the other materials staying constant, there we got a series of WC-Cu based metal powder combinations with decreasing proportion of WC. The designed powder combinations named from #01 to #10 are presented in Table 2.

For the sake of homogeneity of the MMCs, these ten groups of powder mixtures would be mixed in a ball mill separately for at least 8 h in advance of the hot-pressing process. Once the preparatory work was done, all powder mixtures would be filled in a high-strength graphite mold and then compacted in an automatically controlled resistor furnace (SM-100E, Changjiang Jinggong) for hot-pressed sintering, and finally turned into solid cuboids with a theoretical size of 8.5 mm × 8.5 mm × 15 mm. According to past experiences of hot pressing, the higher proportion of WC the harder the composite to be compacted, and that is why the two sets of sintering parameters were implemented in this experiment. Each graphite mold holds 15 composite samples, the compression area of which is 8.5 mm × 15 mm, thus the sintering stress was set 15 MPa with the sintering pressure of 28kN. After all the influential parameters were determined, the hot-pressing process was carried out in accordance with the curve as shown in Fig. 1.

After the matrix samples were manufactured, there followed a pin-on-disc test. Under the same thrust force and wearing time, the sample end-faces in the shape of a square (8.5 mm × 8.5 mm) were worn against grinding wheels perpendicularly through high-speed friction and abrasion tester (MG2000, Kehua Testing Machine, Zhangjiakou, China). In the end, the worn faces of the samples were captured with a scanning electron microscope (SEM, Phenom G2) to get the SEM wear images. And the whole processes of SEM wear image preparation are exhibited in the diagram of Fig. 2.

### 2.2. Matrix wear classification

The purpose of wear classification is to classify various wear phenomena into several basic types so that the research on wear mechanism

**Table 2**

Prescribed powder combinations.

Serial number	Volume fractions of components (vol%)				
	WC	663-Cu	Ni	Co	Mn
#01	50	30	10	5	5
#02	45	35	10	5	5
#03	40	40	10	5	5
#04	35	45	10	5	5
#05	30	50	10	5	5
#06	25	55	10	5	5
#07	20	60	10	5	5
#08	15	65	10	5	5
#09	10	70	10	5	5
#10	5	75	10	5	5

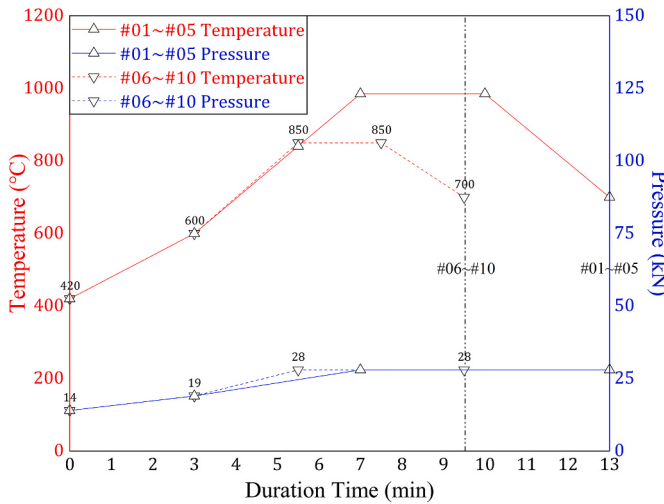


Fig. 1. Hot-pressed sintering curves of powder combinations #1 to #10.

may be classified and it would be easier to explore the essence of wear mechanism. As a result, the quantitative wear evaluation results would be easily applied for correlation analysis between cutting tool qualities and drilling efficiencies, which are planned to be studied in future research. The way of wear classification represents one's understanding of wear mechanism, and appropriate classification would simplify the procedures of studies on wear. However, although enormous wear classification principles have been proposed, there is no one universally accepted. On the basis of previous scholar's studies, classification based on wear mechanisms is considered to be normal and appropriate. The wear classification is of four basic types: abrasive wear, adhesive wear, fatigue wear, and corrosion wear, and their characterization is presented in Table 3.

Combined with the research object in this paper, a sample SEM wear image of WC-Cu based matrix was selected for wear classification illustration since it contains all wear types in this study (abrasive wear, adhesive wear, and fatigue wear). With the utilization of the visualization processing script (`json_to_dataset.py`) in the annotation tool (Labelme, Fig. 4), there got the processed image in the form of wear

masks of the three wear types and wear debris covering on the source image, as the illustration for wear classification in this work (Fig. 3).

The source SEM image as shown in Fig. 3(a) is a gray image with a resolution of  $1088 \times 1024$ , which means that the image has a height of 1088 pixels and a width of 1044 pixels. Each pixel is a value ranging from 0 to 255, representing the grayscale value from pure black (value = 0) to pure white (value = 255). Thus the SEM image could be expressed as a  $1088 \times 1024$  matrix for image processing in the algorithms. And according to the wear classification principle above mentioned, the wear regions on the SEM image of the WC-Cu based metal sample matrix could be divided into four distinguishing classes with different color marked as shown in Fig. 3(b):

- Red for abrasive wear, which means the marked region is characterized by scratches, furrows, grooves, plastic deformation, brittle fracture, or spalling.
- Black for adhesive wear, which means the region is characterized by material migration and adhesion.
- Green for fatigue wear, which means the region is characterized by pits, revolution mark, hit mark, staining mark or features of material falling off.
- Yellow for wear debris, e.g., cutting chips from abrasion, material falling off owing to surface fatigue.

### 2.3. SEM wear image datasets

For wear detection model training with the deep learning method, building the datasets which contain source SEM wear images and their annotation files is always necessary. The annotation files were obtained by manually labeling the wear features of the four classes as marked in Fig. 3(b). Two annotation tools called VGG Image Annotator (VIA) and Labelme were utilized to get the wear annotation files (VIA provides one annotation file containing wear information of all SEM images while Labelme provides one annotation file for one image), and the schematic of wear region labeling is shown in Fig. 4 below. In the actual labeling process, based on the wear classification principle in section 2.2, class labels of "abrasive wear", "fatigue wear" and "wear debris" are included, and that of "adhesive wear" was calculated based on the other two wear types by modifying algorithms, which would be explained in section 2.5.

To make instance segmentation through Mask R-CNN, a training set

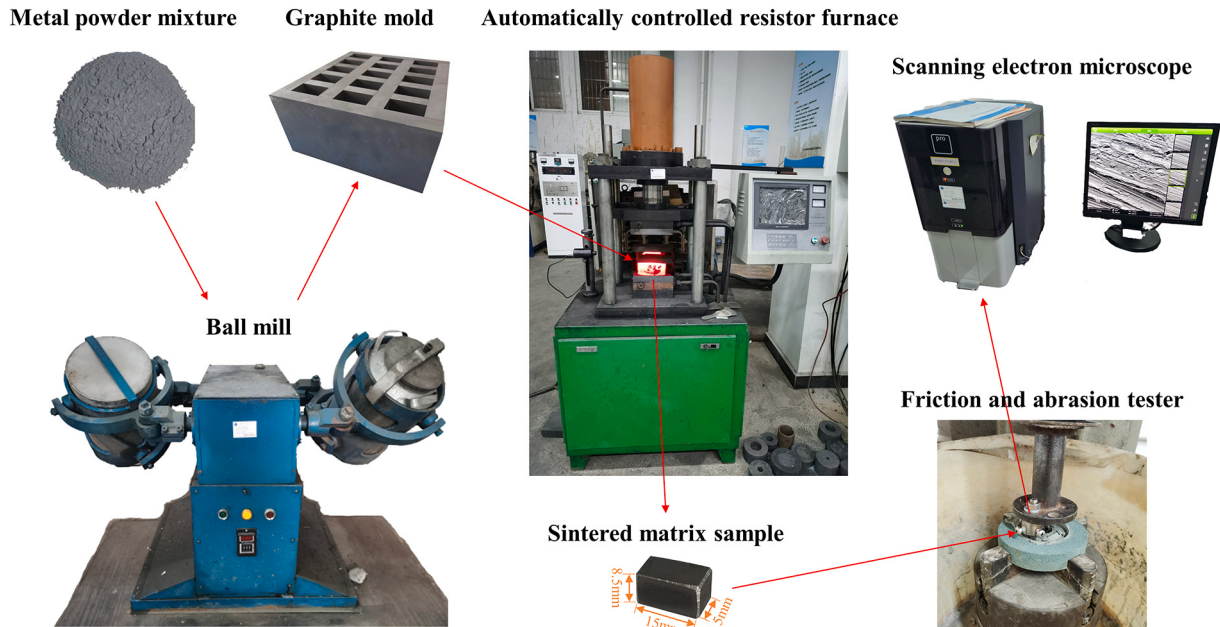


Fig. 2. Diagram of whole processes of SEM wear image preparation.

**Table 3**

Wear classification into four basic types [39].

Wear type	Subclass	Feature description
Abrasive wear	Two-body abrasive wear	there appear scratches, minor furrows, or deep grooves.
	Low-stress abrasive wear	hard surface roughness peak acts as abrasive particles on soft surfaces.
	Three-body abrasive wear	there appears plastic deformation, fatigue, brittle fracture, or spalling.
Adhesive wear	Light adhesive wear	wear is very small and material migration is not significant.
	Common adhesive wear	soft metal adheres to the hard metal surface.
	Scratch	the adhesive material on hard surfaces makes soft surfaces scratched.
Fatigue wear	Scuffing	two surfaces are seriously worn.
	Superficial fatigue wear and Surface fatigue wear	materials fall off and forms wear debris with a smooth fracture.
	Pitting and Peeling	there appears revolution mark, hit mark, staining or other wear mark. wear debris is fan-shaped, and there are many small and deep pits.
Corrosion wear*	Oxidation wear	new surface oxide film forms quickly after the last one got worn away.
	Special corrosive wear	metal surface reacts with acid, alkali, salt, or other medium.
	Fretting	two surfaces are in relative motion with small amplitude.
	Cavitation erosion	surface damage due to relative motion of solid surfaces and liquids.

\* Corrosion wear is not involved in the condition of this study.

should always be prepared first for model training, and a validation set would be set to avoid over-fitting, besides, there should be a test set to check the generation ability of the model. In this way, the obtained SEM wear images could be divided into three groups — the first two groups of images were marked on wear regions with labels of the three wear types, and they constituted the training set and validation set with annotation files respectively; the last group constituted the test set with no need of annotation files. In this work, 1040 SEM wear images were distributed into training, validation and test sets as shown in Table 4, where every

dataset contains all powder combinations.

#### 2.4. Mask R-CNN framework

In the case of image detection, CNNs capture the spatial features, which refers to the arrangement of pixels in the image and the relationships among them. They can help us accurately identify the area, position of one object, and its relationship with other objects. Compare to conventional Artificial Neural Networks (ANNs), CNNs use filter kernels as the building block to extract features from the input files by convolution processing. From R-CNN (2014) [40] to Fast R-CNN (2015) [41] and Faster R-CNN (2016) [42], CNNs have shown rapid improvement of object detection performance year by year. Moreover, by adding a branch for object mask predicting in parallel with the existing branch for bounding box recognition (Fig. 5), the Faster R-CNN was extended to be the Mask R-CNN (2017) [26] efficient for object instance segmentation.

Mask RCNN is a two-stage framework: the first stage scans the input images and generates the proposals, while the second classifies the proposals, generates the bounding boxes and masks. Architecture the Mask R-CNN in Fig. 6 reveals its computing process, where the main work could be divided into 6 components [43]:

(a) Feature Extraction Network was used as the backbone to extract wear features from the input image and provide the feature maps, which were evaluated by (b) Region Proposal Network (RPN) to propose the bounding boxes of the ROI, then (c) Region of Interest Alignment (RoI Align) refined the extracted regions to improve the alignment. Using a small artificial neural network (ANN) of fully connected layers (FC layers), the (d) Bounding Box Regression Block handled the regression of the bounding boxes, and the (e) Instance Classification Block classified all instances. For instance segmentation processes in the (f) Instance Segmentation Block, the segmentation process was achieved by a pixel-based binary classification based on a small CNN, where each pixel was assigned one of the predetermined label classes.

#### 2.5. Detection result processing

As an end-to-end instance segmentation method, Mask R-CNN has shown great advantages relative to detect-then-segment approaches. For

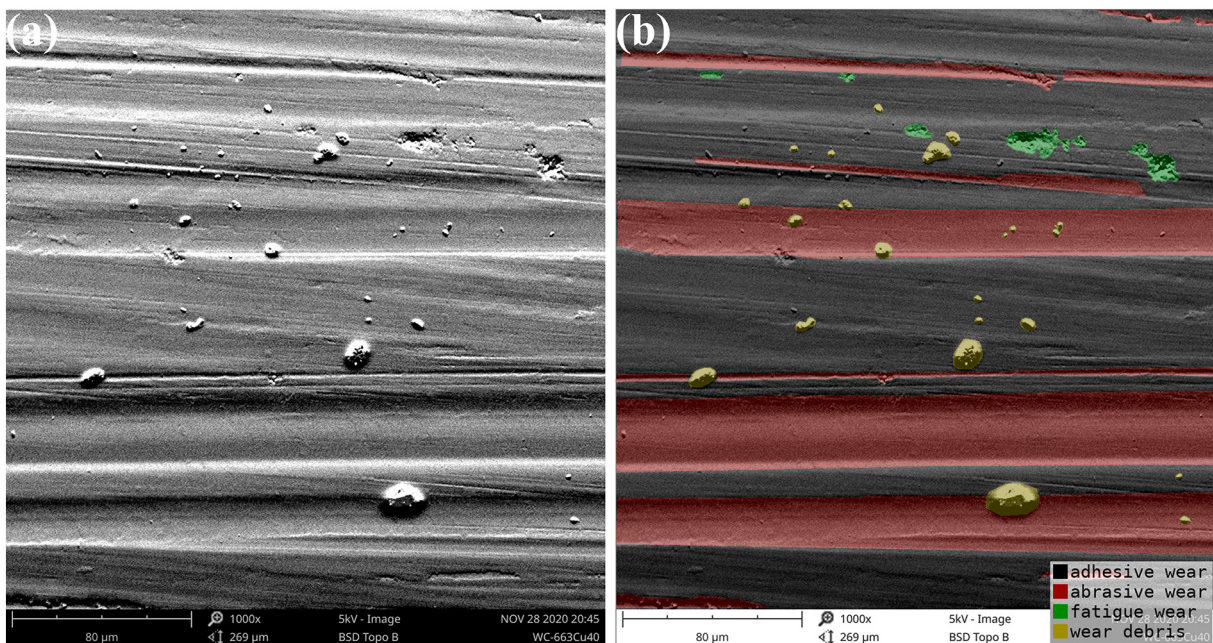


Fig. 3. Wear classification principle illustration: (a) Sample SEM wear image; (b) Classification of wear regions.

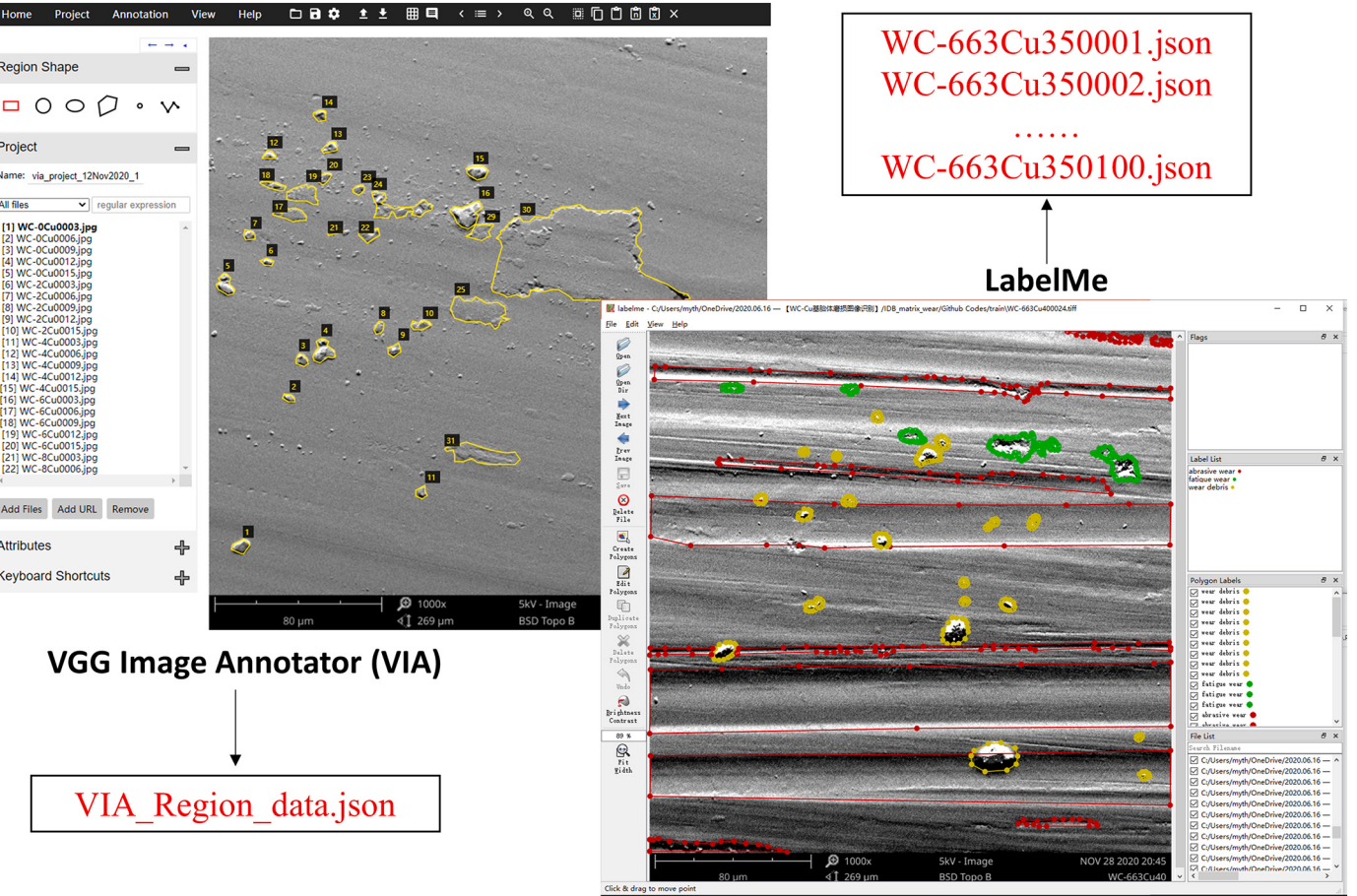


Fig. 4. Schematic of wear region labeling with annotation tools.

every input wear image, the trained Mask R-CNN model could provide segmentation results directly. For the sample SEM wear image in Fig. 3(a), after wear detection processing through the trained Mask R-CNN model, the output wear prediction result, in the form of source image covered with segmented instances marked in different colors, was obtained as shown in Fig. 7(a). It could be noticed from Fig. 3(a) to Fig. 7(a) that multiple regions on the source SEM image got labelled with masks in bounding boxes with different colors. As referred to as instance segmentation, Mask R-CNN provides such prediction results for every input image, where each piece of the region covered with a mask in one color is called an instance (predicted one). Every instance attached with a bounding box represents a region full of the features of one certain class we defined in the labeling process, and the predicted instances are separate from each other. Therefore, there is an instance, there is a kind of color (determined randomly by the algorithms) on the output image in Fig. 7(a), which is what we can get directly from such an end-to-end network, besides, the information of every instance can be accessed in the form of a matrix from the algorithms.

However, for our purpose in this paper, there is no need to count how many wear instances the Mask R-CNN model would be detected, and we only wish to get the wear regions of the same class (there are total four classes: abrasive wear, adhesive wear, fatigue wear and wear debris). As Fig. 7(b) shows, instances in the same wear types were re-marked as the same color according to the instruction in Fig. 3(b) — red for abrasive wear, black for adhesive wear, green for fatigue wear, and yellow for wear debris, in other words, the four classes of objects were segmented. Within the Mask R-CNN algorithms for wear detection, the masks of detected instances are expressed as Boolean matrices, possessing the same resolution as the corresponding source images. Thus by modifying the algorithm, the masks of wear region due to abrasion, adhesion and

fatigue could be extracted and then added up to obtain the wear masks of the three wear types, i.e., abrasive wear mask presented in Fig. 7(c), adhesive wear mask in Fig. 7(d), and fatigue wear mask in Fig. 7(e), moreover, the sizes and distributions of wear debris could also be accessed as shown in Fig. 7(f).

In our expectation, the identified region masks of abrasive, adhesive and fatigue wear added up could occupy the whole screen of the visual field of the metal matrix (with a resolution of  $1024 \times 1024$ ), and the wear debris mask was separate floating on all of them. As mentioned in section 2.3, the region mask of adhesive wear would be obtained by calculating the wear region remainder apart from the abrasive wear and fatigue wear. However, the wear debris would cause a lot of trouble because of the wear identification method based on wear regions marked with different colors, and this is one of the reasons why instance segmentation instead of semantic segmentation (one pixel indicates one class of object) was chosen for wear detection. For the wear region mask combination exhibited in Fig. 7(b) and there in Fig. 8(a), the processing results of semantic segmentation and instance segmentation are shown in Fig. 8(b) and Fig. 8(c).

Since only the class labels of abrasive wear, fatigue wear and wear debris were involved in the annotation files, the final produced detection results just contain instances of these three classes as well. The Mask R-CNN model makes it possible to process wear debris separately, resulting in instance masks of wear debris floating on masks of the three wear types as we hope. However, it also induced the problem of overlap between instance masks of the same wear types. It could be noticed from the region annotated with white boxes on the image in Fig. 9(a) that the detection on abrasive wear got repeated wrongly, which may lead to statistical error due to repeated calculation and thus pull down the effects of pixel-level recognition and classification. In this regard, masks of

**Table 4**  
SEM wear images distributed into training, validation and test sets.

Serial number	SEM wear image name	Total	Training set	Validation set	Test set
#01 (50 vol% WC)	WC-663Cu300001 ~ WC-663Cu300090	90	50	30	10
#02 (45 vol% WC)	WC-663Cu350001 ~ WC-663Cu350090	90	50	30	10
#03 (40 vol% WC)	WC-663Cu400001 ~ WC-663Cu400096	96	50	30	16
#04 (35 vol% WC)	WC-663Cu450001 ~ WC-663Cu450132	132	50	30	52
#05 (30 vol% WC)	WC-663Cu500001 ~ WC-663Cu500102	102	50	30	22
#06 (25 vol% WC)	WC-663Cu550001 ~ WC-663Cu550096	96	50	30	16
#07 (20 vol% WC)	WC-663Cu600001 ~ WC-663Cu600096	96	50	30	16
#08 (15 vol% WC)	WC-663Cu650001 ~ WC-663Cu650107	107	50	30	27
#09 (10 vol% WC)	WC-663Cu700001 ~ WC-663Cu700098	98	50	30	18
#10 (5 vol % WC)	WC-663Cu750001 ~ WC-663Cu750133	133	50	30	53
(total 1040 SEM images (1088 × 1024) in TIFF format)		1040	500	300	240

the same wear type were merged by taking the union of their masks, and the example treatment is also exhibited as drawn there.

In this way, we got the masks of abrasive wear, fatigue wear and wear debris separately, which could be indicated in Fig. 7(c), Fig. 7(e), and Fig. 7(f) respectively. While wear debris mask would be calculated separately, only the ascription of overlap between abrasive wear mask and fatigue wear mask needs to be taken into consideration, while the adhesive wear mask can be determined no matter which one the overlap region belongs to. As a result, the wear region distribution on the SEM image could be indicated as shown in Fig. 9(b). In our prospect of the research, different types of wear may be related to different mechanisms and degrees of wear failure of the MMC tools, and they would make

great impacts on the drilling performance of impregnated diamond bits. By counting the region area of every wear mask and treating the overlap region as detection errors on this SEM wear image, there we got its wear mode referring to the combination of abrasive wear (area range of  $S_A \sim S_{A+B}$ ), adhesive wear (area of region  $S_D$ ), and fatigue wear (area range of  $S_C \sim S_{B+C}$ ). It was inferred that the overlap region between abrasive wear and fatigue wear comes from its morphologies which may be similar in wear conditions of adhesion and fatigue, for example, the similarity between grooves (abrasive wear) and pits (fatigue wear). In any case, the influences of different wears would thus be easier to be studied with detailed and accurate quantitative wear data in further studies.

### 3. Results and discussion

#### 3.1. Wear detection performance

For a demonstration of wear detection making use of the trained Mask R-CNN model, six SEM images published in previous work [38] were added into the test set for prediction, or in other words inference, to output the information to be gained from them. The detection results and their quantitative statistics are presented in Fig. 10 and Table 5 respectively.

According to the wear classification principle prescribed in section 2.2, the Mask R-CNN model would make effective identification among abrasive wear, fatigue wear and wear debris through their key features as Fig. 10 shows. Afterward, based on the detection result processing method explained in section 2.5, the quantitative statistics of all the four classes (include adhesive wear in addition to the first three) could be calculated as listed in Table 5, which can well support the qualitative description (no repetition here) in the source literature [38]:

The wear mode of sample(a) was fatigue wear ( $2053.85 \mu\text{m}^2$ ) and adhesive wear ( $70,307.34 \mu\text{m}^2$ ).

The wear mode of sample(b) was adhesive wear ( $69,375.78 \mu\text{m}^2$ ) and abrasive wear ( $2985.40 \mu\text{m}^2$ ).

The wear mode of sample(c) was abrasive wear ( $1550.22 \mu\text{m}^2$ ) and adhesive wear ( $70,810.96 \mu\text{m}^2$ ).

The wear mode of sample(d) was abrasive wear ( $5619.13 \mu\text{m}^2$ ) and adhesive wear ( $66,742.05 \mu\text{m}^2$ ).

The wear mode of sample(e) was abrasive wear ( $4539.34 \sim 4678.95 \mu\text{m}^2$ ), fatigue wear ( $3.24 \sim 142.85 \mu\text{m}^2$ ), and adhesive wear ( $67,678.99$ ). The detection error between abrasive wear and fatigue wear is  $139.61 \mu\text{m}^2$ .

The wear mode of sample(f) abrasive wear ( $1875.39 \mu\text{m}^2$ ) and

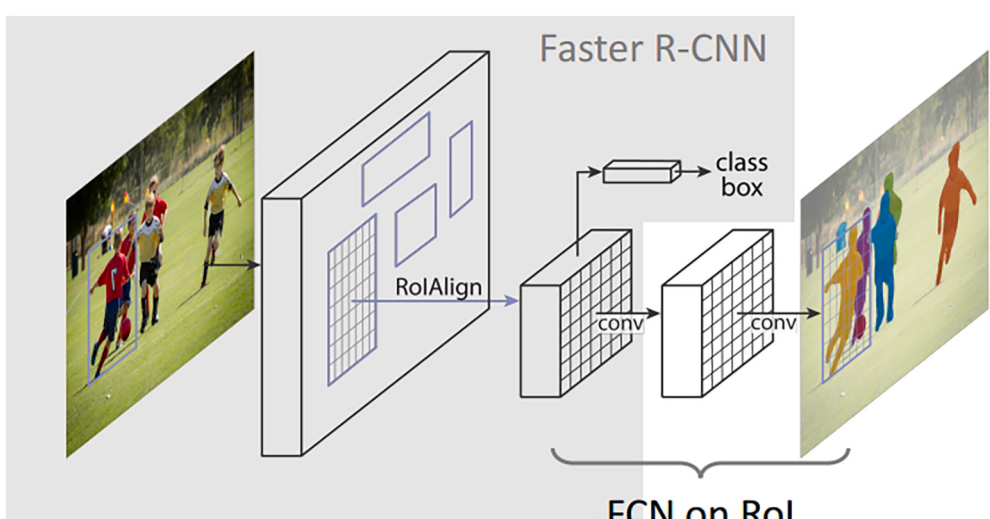


**Fig. 5.** Mask R-CNN extended from Faster R-CNN.

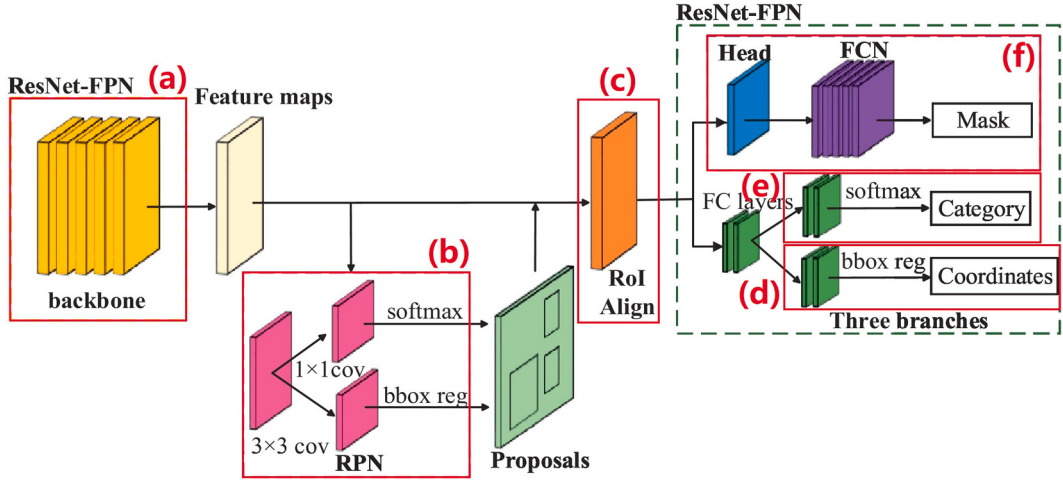


**Fig. 6.** The architecture of Mask R-CNN [28].

(a) Feature Extraction Network (backbone), (b) Region Proposal Network, (c) Region of Interest Alignment, (d) Bounding Box Regression Block, (e) Instance Classification Block, (f) Instance Segmentation Block.

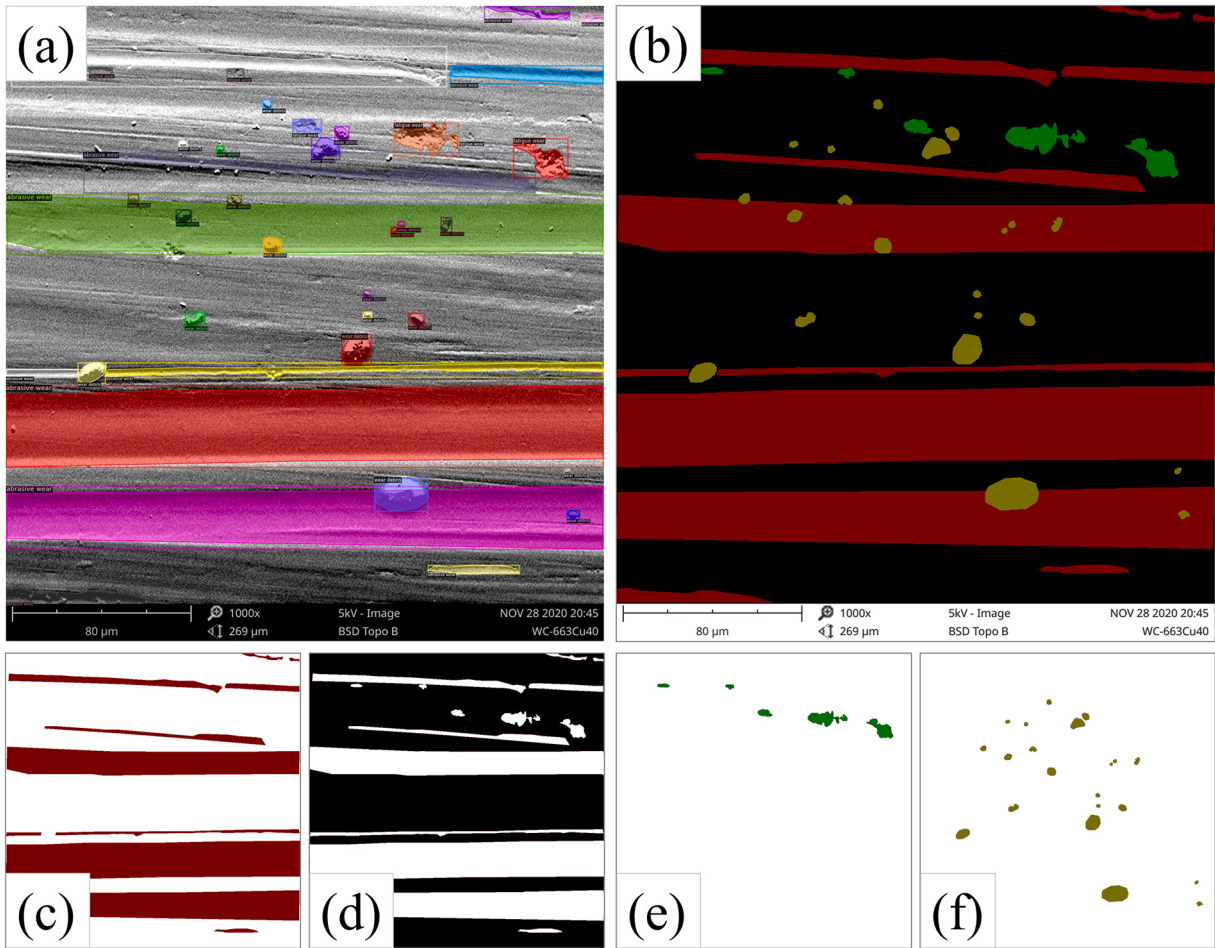


**Fig. 7.** Wear region mask extraction based on detection results.

(a) Wear detection result; (b) Wear regions sorted out as four classes; (c) Abrasive wear mask; (d) Adhesive wear mask; (e) Fatigue wear mask; (f) Wear debris mask.

adhesive wear ( $70,485.79 \mu\text{m}^2$ ).

### 3.2. Mask R-CNN model evaluation

For every SEM image in the training set, there we can obtain two

processed images, attached with instances identified by ground truth and model detection, as marked in Fig. 11(a) and Fig. 11(b) respectively. The term “ground truth” refers to the identification results from manual labeling, as the reference to determine whether there are features of some wear types on certain regions. Features like this extracted from the

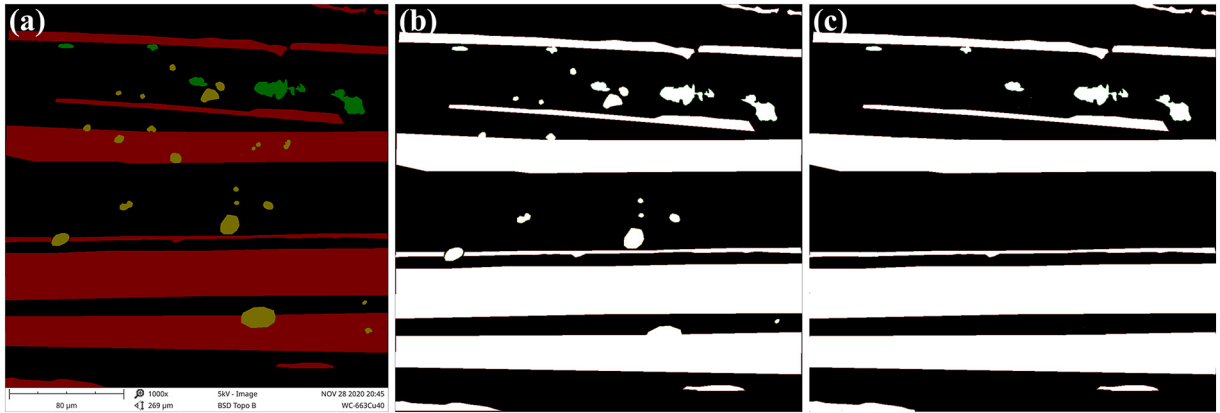


**Fig. 8.** Adhesive wear mask processing.  
(a) Wear region mask combination; (b) Semantic segmentation result; (b) Instance segmentation result.

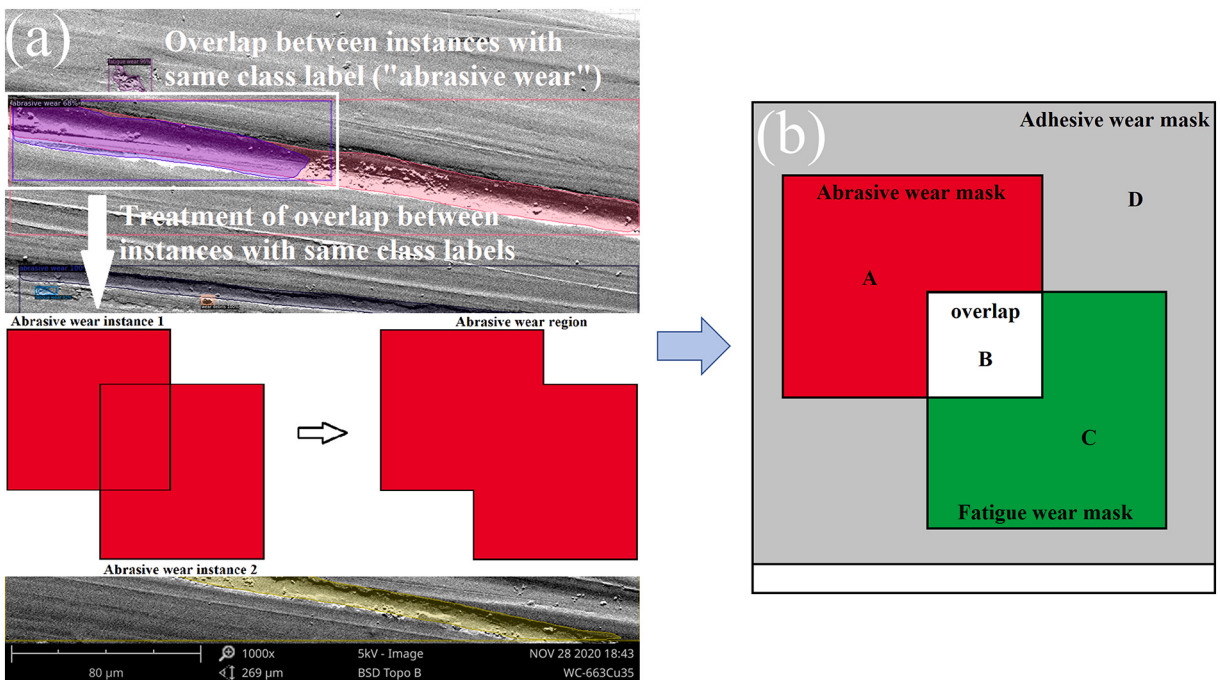


**Fig. 9.** Treatment of wear region overlap.  
(a) Overlap between same class label instance masks; (b) Overlap between different class wear masks.

images in the training set formed the wear identification principle of the Mask R-CNN model, and thereafter the detection results of the input image were output. For the ground truth as shown in Fig. 11(a), there are four instances of wear debris labelled on the SEM wear image, however, the detected wear debris instances are much more detailed (eight instances were detected) as shown in Fig. 11(b). In fact, as a kind of “reference answer” to the question of what the wear mode on the SEM wear image is, ground truth on single wear image may not be right (reference answers differ from people to people), but their combination would be way more thorough and precise. What’s more, in the algorithms, the wear identification principle of the trained Mask R-CNN model was the weights and bias trained through these ground truths. As a result, deep learning showed a significant superiority over artificial identification in wear detection on SEM images.

Suppose that the predicted result of the upper wear debris instance in Fig. 11(b) has a distinguishable difference with that in Fig. 11(a) (simplified as in Fig. 12), and thus the instance detection results can be divided into four kinds:

TP (True Positive): the sample is positive in the ground truth and was predicted correctly.

TN (True Negative): the sample is negative in the ground truth and was predicted correctly.

FP (False Positive): the sample is negative in the ground truth but was predicted wrongly as the positive.

FN (False Negative): the sample is positive in the ground truth but was predicted wrongly as the negative.

Moreover, for object detection in deep learning, precision, recall, accuracy, and IoU(Intersection over Union) are important indexes for the training process based on the above four. They can be obtained by calculation as the equations shown in Eq. (1)(2)(3)(4), where  $N$  refers to sample number and  $S$  for sample area.

$$\begin{aligned} \text{precision (P)} &= \frac{\text{number of positive samples correctly predicted}}{\text{number of total predicted samples}} \\ &= \frac{N_{\text{TP}}}{N_{\text{TP}} + N_{\text{FP}}} \end{aligned} \quad (1)$$

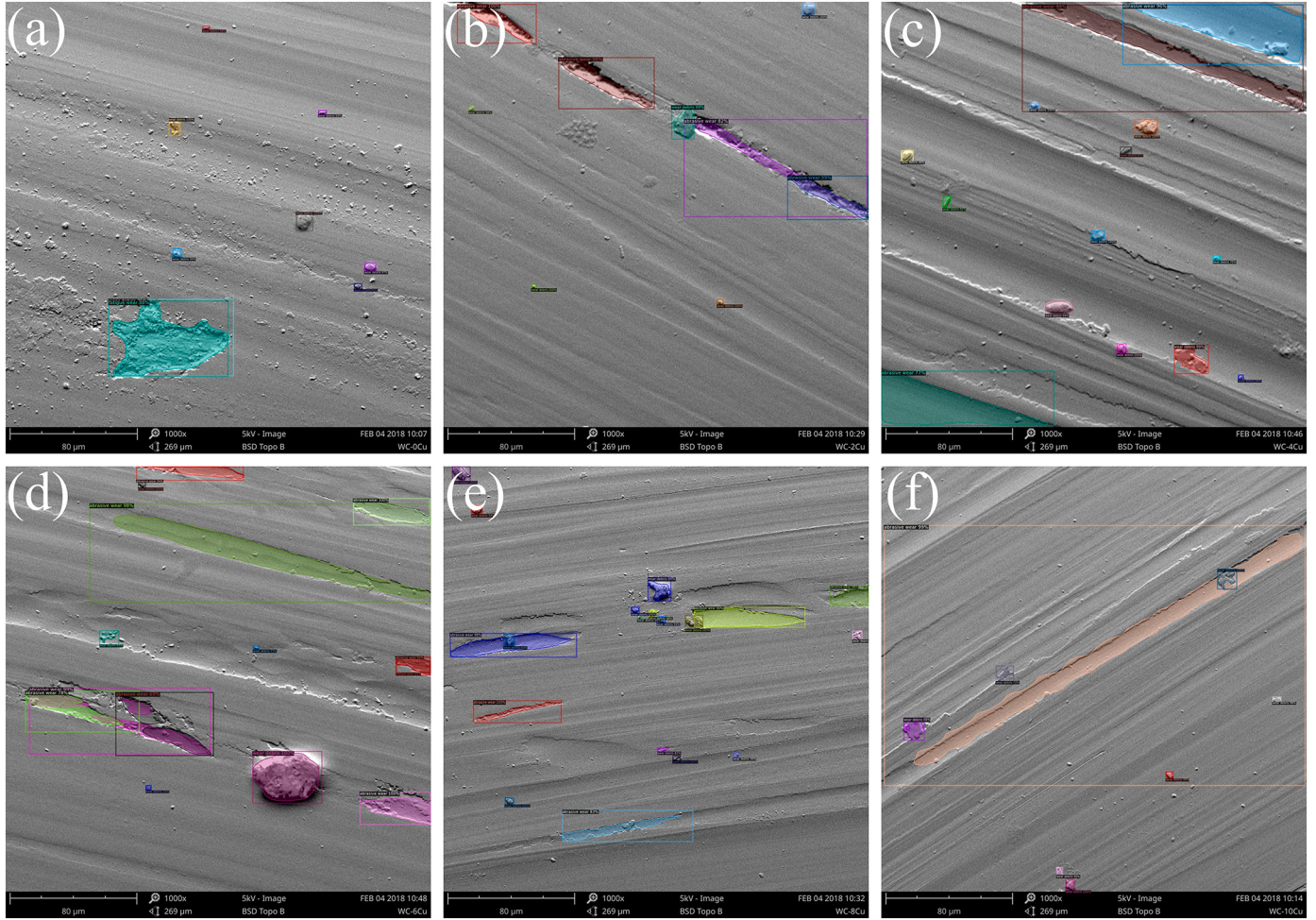


Fig. 10. Detection results of six published wear images.

**Table 5**  
Quantitative statistics of detection results in Fig. 10 (generated directly from the modified algorithms).

Sample number	Power combination	Instance number	Wear region area <sup>a</sup> ( $\mu\text{m}^2$ )			
			Abrasive wear	Overlap	Fatigue wear	Adhesive wear
(a)	#01 (50 vol% WC)	9	0	0	2053.85	70,307.34
(b)	#02 (45 vol% WC)	8	2985.40	0	0	69,375.78
(c)	#03 (40 vol% WC)	9	1550.22	0	0	70,810.96
(d)	#04 (35 vol% WC)	14	5619.13	0	0	66,742.05
(e)	#05 (30 vol% WC)	14	4539.34–4678.95	139.61	3.24–142.85	67,678.99
(f)	#06 (25 vol% WC)	19	1875.39	0	0	70,485.79

\* SEM images involved in this study were captured with a magnification of x1000, getting a visual scope of  $269 \mu\text{m} \times 269 \mu\text{m}$  at a resolution of  $1024 \times 1024$ , thus every pixel on the SEM image represents a piece of region occupying about  $0.069 \mu\text{m}^2$ .

$$\text{recall (R)} = \frac{\text{number of positive samples correctly predicted}}{\text{number of total predicted samples}} = \frac{N_{TP}}{N_{TP} + N_{FN}} \quad (2)$$

$$\begin{aligned} \text{accuracy (A)} &= \frac{\text{number of samples correctly classified}}{\text{number of total samples}} \\ &= \frac{N_{TP} + N_{TN}}{N_{TP} + N_{TN} + N_{FP} + N_{FN}} \end{aligned} \quad (3)$$

$$\text{IoU} = \frac{\text{area of overlap}}{\text{area of union}} = \frac{S_{TP}}{S_{TP} + S_{FP} + S_{FN}} \quad (4)$$

In the algorithm of the Mask R-CNN framework, the IoU was defined for evaluation of predicted instance and thus adjusting the Mask R-CNN

model parameters, and a threshold value of it is usually set to judge whether the sample is correctly detected. Precision and recall are also important parameters — the first one indicates how many samples in the prediction results were correct, and the second one reflects how many positive samples were correctly detected in prediction results. When precision reaches up to 100%, it means that there is no error detection, and for recall, it indicates that there is no missed detection. For demonstration to this research, 100 images were trained for 10,000 steps, their training data were processed into the three evolution curves relative to the training steps as shown in Fig. 13(a), Fig. 13(b), and Fig. 13(c). It could be noticed that the more training steps, the better detection accuracy, and naturally the lower proportions of FP and FN.

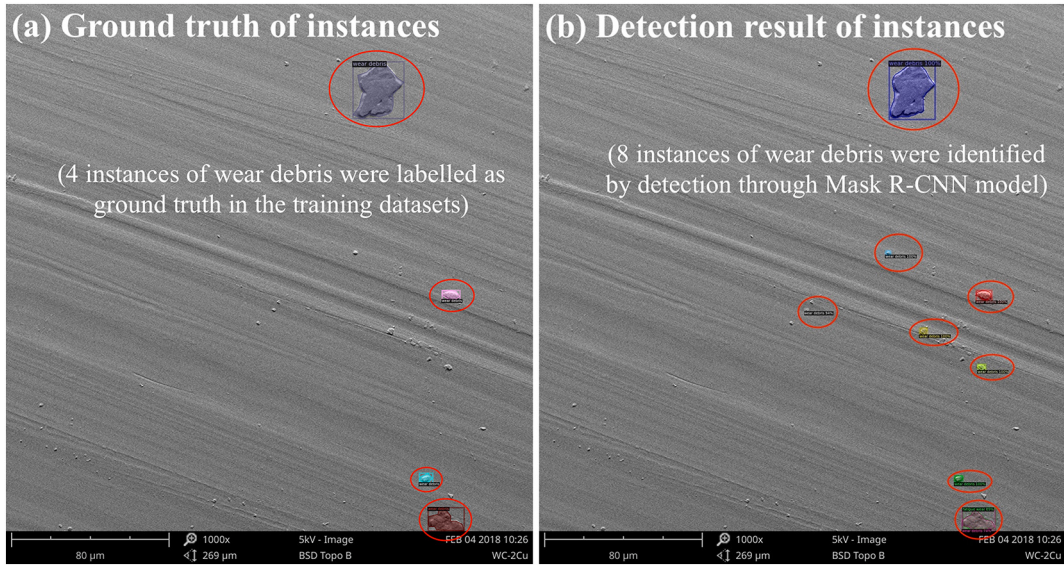


**Fig. 11.** Wear instance identification in ground truth vs detection result.

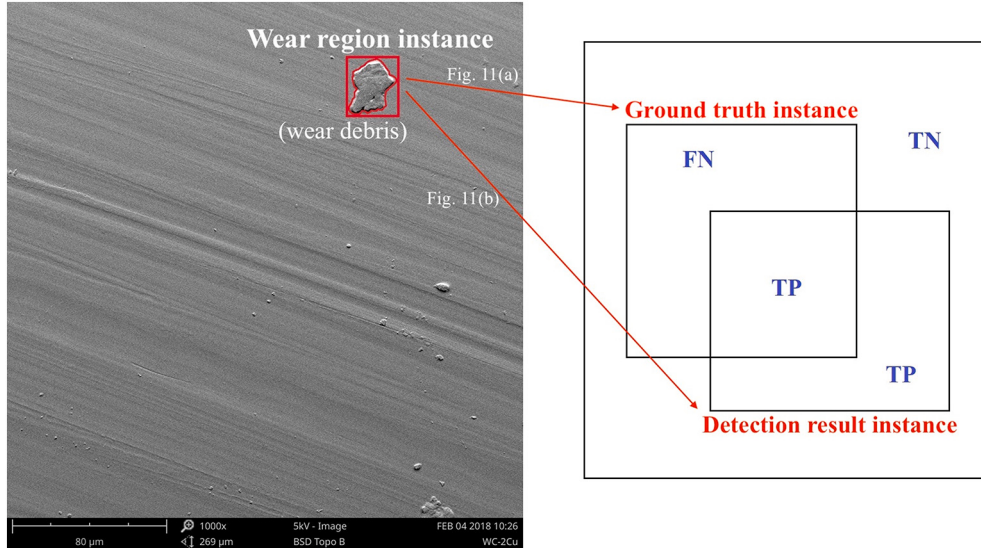


**Fig. 12.** Wear detection accuracy evaluation indexes.

### 3.3. Wear region mask evaluation

And for wear detection performance, these 100 SEM wear images were examined for model effectiveness evaluation. Based on Eq.(4), there we proposed a new evaluation index, mask IoU as obtained by Eq. (5) according to the wear region mask extraction method exhibited in Fig. 7(c)(d)(e)(f). In other words, we used masks of the four classes of wear objects (i.e., abrasive wear, adhesive wear, fatigue wear, and wear debris) instead of their single detected instances for calculation of the IoU. Moreover, by getting the difference divided by the sum of class areas, there we can get the area loss of this class of object by Eq. (6), where  $S$  refers to the mask area. It should be noticed that the mask overlap between abrasive wear and fatigue as had been explained in Fig. 9 does not influence these two parameters since the masks are utilized for accuracy analysis here.

$$\text{mask IoU} = \frac{\text{area of overlap}}{\text{area of union}} = \frac{S_{\text{ground truth mask}} \cap S_{\text{prediction result mask}}}{S_{\text{ground truth mask}} \cup S_{\text{prediction result mask}}} \quad (5)$$

$$\text{area loss} = \frac{\text{difference of area}}{\text{sum of area}} = \frac{S_{\text{ground truth mask}} - S_{\text{prediction result mask}}}{S_{\text{ground truth mask}} \cup S_{\text{prediction result mask}}} \quad (6)$$

Therefore, the mask IoU and area loss of the three wear types and the wear debris can be calculated separately and plotted as point maps as presented in Fig. 14. The higher the mask IoU and the lower the area loss, the better the training effect. As the graphs show, the data points are mainly distributed in the lower right corner, which means the overall performance of the trained model is well enough to meet the requirement of wear detection.

Moreover, for statistical analysis of the detection performance evaluation of abrasive, adhesive, fatigue wear and wear debris, the data presented in Fig. 14 are counted into a box plot (Fig. 15). Besides, the key values in the box plot were counted in Table 6. As the plot in Fig. 15 reveals, 100 image sample were examined for mask IoU and area loss of the four classes of objects respectively, and the mean value and quartile values (25% for the lower quartiles, 50% for the median, and 75% for the upper quartiles) were presented in Table 6. As it had been illustrated that higher mask IoU and lower area loss represent better training

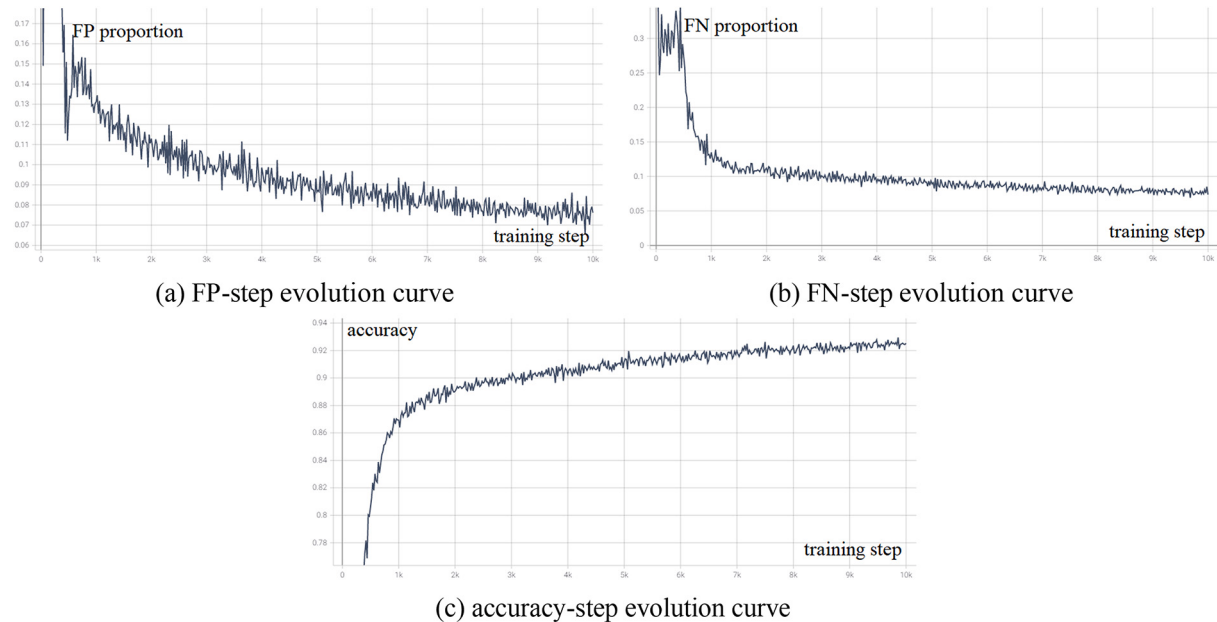


**Fig. 13.** Evolution curve curves between model evaluation indexes and training steps.

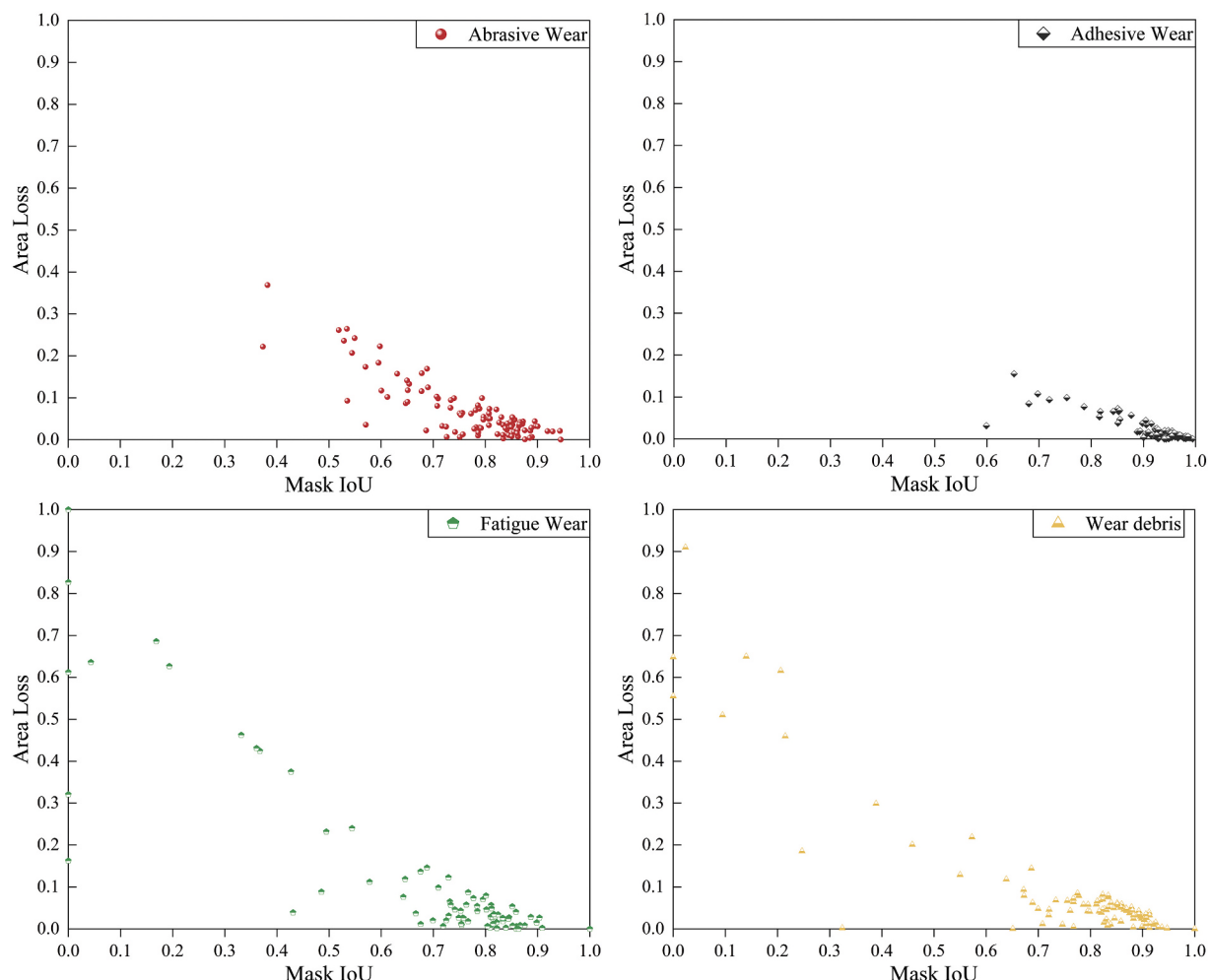


**Fig. 14.** Distribution map of area loss and mask IoU of the four class labels.

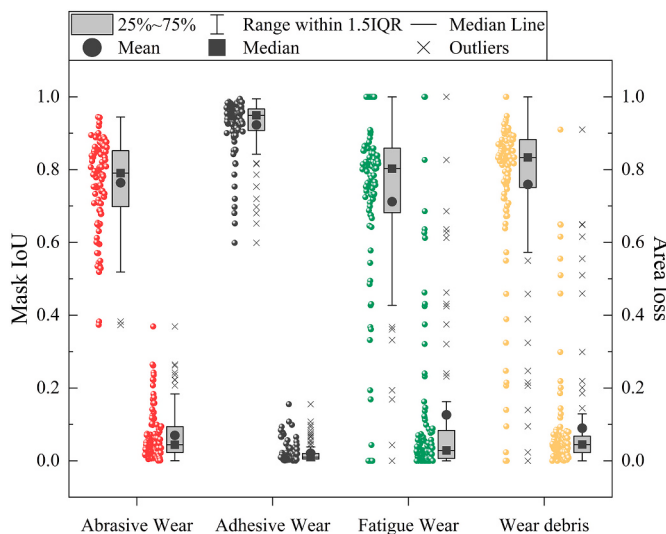


**Fig. 15.** Statistical analysis of mask IoU and area loss.

effects, here the 25% value of mask IoU and 75% value of area loss were used as the criterion parameters respectively. As a result, the detection of abrasive wear showed the mask IoU of 70.26% and the area loss of 2.32%. In like manner, the adhesive wear has a mask IoU of 90.85% and an area loss of 0.48%, the fatigue wear has a mask IoU of 68.47% and an area loss of 0.64%, and those of wear debris are 75.34% and 2.25%. In a conclusion, the average wear region mask IoU is nearly over 70%, and the average wear region area loss is no more than 3%. The evaluation results showed that the recognition effect of the model trained with deep learning algorithms has high accuracy and low error.

#### 4. Conclusions

To evaluate the wear of metal matrix quantitatively and normatively, a series of WC-Cu based MMC samples were manufactured with hot-pressed sintering. After the pin-on-disc test, the SEM wear images of the worn surface were obtained, based on which the datasets for training, validation and test were established. In the utilization of Mask R-CNN algorithms, a wear detection model had been trained and showed excellent performance in recognition and evaluation of wear regions, and the main conclusions are drawn as follows:

- (1) The detection results of the Mask R-CNN model showed that the deep learning method is feasible in the recognition and evaluation of MMC wear. The three kinds of wear, i.e., abrasive, adhesive, and fatigue wear, were accurately identified and marked, as the output detection results with bounding boxes, masks, class labels, and confidences attached. The test on published wear images showed good performance of quantitative statistics of wear.
- (2) Extracting the wear region mask of the same type of wears, there we proposed mask IoU and area loss for wear evaluation. In the test with 100 SEM images, the average wear region mask IoU is over 70%, and the average wear region area loss is no more than 3%, which means the recognition effect of the model trained with deep learning algorithm meets the requirement of WC-Cu based matrix wear identification with high accuracy and low error.
- (3) By modifying the algorithms, there we obtained the wear mode of tested SEM wear image with quantitative data, i.e., of abrasive wear, adhesive wear and fatigue wear combinations with specific region areas, based on which the functional relationship between MMC wear indexes and IDB drilling performance such as rate of penetration (ROP) is planned to be studied in further research.

**Table 6**

Key values of mask IoU and area loss in Fig. 15.

Evaluation Index	Abrasive wear	Adhesive wear	Fatigue wear	Wear debris
mask IoU*	Mean value	76.37%	92.26%	71.20%
	75% value	85.21%	96.64%	85.88%
	Median value	79.02%	94.91%	80.27%
	25% value	70.26%	90.85%	68.47%
area loss*	Mean value	6.98%	2.06%	12.62%
	75% value	9.32%	1.98%	8.12%
	Median value	4.38%	1.01%	2.84%
	25% value	2.32%	0.48%	0.64%

\* Average mask IoU of every single class is represented by the upper quartiles, and area loss by the lower quartiles respectively.

Supplementary data to this article can be found online at <https://doi.org/10.1016/j.ijrmhm.2021.105530>.

#### Data and code availability

The codes and datasets are available at [https://github.com/sunwucheng/IDB\\_matrix\\_wear](https://github.com/sunwucheng/IDB_matrix_wear).

The training, validation, and test processes are repeatable online with the codes open-sourced there.

#### Declaration of Competing Interest

The authors declare that they have no known competing financial interests or personal relationships that could have appeared to influence the work reported in this paper.

#### Acknowledgments

This study was supported by the National Natural Science Foundation of China (contract no. 41972327) and the External Cooperation Program of Science and Technology Department of Hubei Province (no. 2019AHB051).

#### References

- [1] H. Xie, H. Konietzky, H.W. Zhou, Special issue “deep mining,” Rock Mech. Rock Eng. 52 (2019) 1415–1416, <https://doi.org/10.1007/s00603-019-01805-9>.
- [2] H. Wagner, Deep mining: a rock engineering challenge, Rock Mech. Rock. Eng. 52 (2019) 1417–1446, <https://doi.org/10.1007/s00603-019-01799-4>.
- [3] J. Limberger, T. Boxem, M. Pluymaekers, D. Bruhn, A. Manzella, P. Calcagno, F. Beekman, S. Cloetingh, J.-D. van Wees, Geothermal energy in deep aquifers: a global assessment of the resource base for direct heat utilization, Renew. Sust. Energ. Rev. 82 (2018) 961–975, <https://doi.org/10.1016/j.rser.2017.09.084>.
- [4] S. Tan, X. Fang, K. Yang, L. Duan, A new composite impregnated diamond bit for extra-hard, compact, and nonabrasive rock formation, Int. J. Refract. Met. Hard Mater. 43 (2014) 186–192, <https://doi.org/10.1016/j.ijrmhm.2013.11.001>.
- [5] W. Tillmann, Trends and market perspectives for diamond tools in the construction industry, Int. J. Refract. Met. Hard Mater. 18 (2000) 301–306, [https://doi.org/10.1016/S0263-4368\(00\)00034-2](https://doi.org/10.1016/S0263-4368(00)00034-2).
- [6] H.K. Tönshoff, H. Hillmann-Apmann, J. Asche, Diamond tools in stone and civil engineering industry: cutting principles, wear and applications, Diam. Relat. Mater. 11 (2002) 736–741, [https://doi.org/10.1016/S0925-9635\(01\)00561-1](https://doi.org/10.1016/S0925-9635(01)00561-1).
- [7] P. Flegner, J. Kacur, M. Durdán, M. Laciák, B. Stehlíková, M. Pástor, Significant damages of core diamond bits in the process of rocks drilling, Eng. Fail. Anal. 59 (2016) 354–365, <https://doi.org/10.1016/j.engfailanal.2015.10.016>.
- [8] T. Xuefeng, T. Shifeng, The wear mechanisms of impregnated diamond bits, Wear. 177 (1994) 81–91, [https://doi.org/10.1016/0043-1648\(94\)90120-1](https://doi.org/10.1016/0043-1648(94)90120-1).
- [9] C. Gao, J. Yuan, H. Jin, Z. Song, Wear characteristics of impregnated diamond bit in drilling armor ceramic, in: G. Zhu (Ed.), Mater. Sci. Eng. Pts 1–2, Trans Tech Publications Ltd, Laublsrutistr 24, CH-8717 Stafa-Zurich, Switzerland, 2011, pp. 1150–1155, <https://doi.org/10.4028/www.scientific.net/AMR.179-180.1150>.

- [10] A. Gupta, S. Chattopadhyaya, S. Hloch, Critical investigation of wear behaviour of WC drill bit buttons, *Rock Mech. Rock. Eng.* 46 (2013) 169–177, <https://doi.org/10.1007/s00603-012-0255-9>.
- [11] L. Zheng, H. Huan, Y. Zeng, S. Song, S. Cheng, C. Zhang, A study on the failure mechanism and wear loss of impregnated diamond bits during machining process of armor ceramics, *J. Mech. Sci. Technol.* 32 (2018) 261–268, <https://doi.org/10.1007/s12206-017-1226-6>.
- [12] M. Mostofi, T. Richard, L. Franca, S. Yalamanchi, Wear response of impregnated diamond bits, *Wear.* 410–411 (2018) 34–42, <https://doi.org/10.1016/j.wear.2018.04.010>.
- [13] D. Miller, A. Ball, The wear of diamonds in impregnated diamond bit drilling, *Wear.* 141 (1991) 311–320, [https://doi.org/10.1016/0043-1648\(91\)90276-Z](https://doi.org/10.1016/0043-1648(91)90276-Z).
- [14] S. Li, Q. Xiang, L. Zhang, The wear mechanisms of diamond impregnated bit matrix, in: J. Li (Ed.), *Mach. Electron. Control Eng. III*, Trans Tech Publications Ltd, Laublsrutiststr 24, CH-8717 Stafa-Zurich, Switzerland, 2014, pp. 15–18, <https://doi.org/10.4028/www.scientific.net/AMM.441.15>.
- [15] A.J. Gant, I. Konyashin, B. Ries, A. McKie, R.W.N. Nilen, J. Pickles, Wear mechanisms of diamond-containing hardmetals in comparison with diamond-based materials, *Int. J. Refract. Met. Hard Mater.* 71 (2018) 106–114, <https://doi.org/10.1016/j.ijrmhm.2017.10.013>.
- [16] X. Zhao, L. Duan, A review of the diamond retention capacity of metal bond matrices, *Metals.* 8 (2018) 307, <https://doi.org/10.3390/met8050307>.
- [17] P.S.M. Dougherty, R. Pudjoprawoto, C. Fred Higgs, Bit cutter-on-rock tribometry: analyzing friction and rate-of-penetration for deep well drilling substrates, *Tribol. Int.* 77 (2014) 178–185, <https://doi.org/10.1016/j.triboint.2014.04.003>.
- [18] S. Pelletier, M. Dufour, Characterization of wear and profile of diamond drill bit by optical profilometry, *Rev. Sci. Instrum.* 65 (1994) 208–211, <https://doi.org/10.1063/1.1144787>.
- [19] L. Peng, B. Pan, Z. Liu, Z. Liu, S. Tan, Investigation on abrasion-corrosion properties of WC-based composite with fractal theory, *Int. J. Refract. Met. Hard Mater.* 87 (2020) 105142, <https://doi.org/10.1016/j.ijrmhm.2019.105142>.
- [20] N. Malevich, C. Müller, J. Dreier, M. Kansteiner, D. Biermann, M. De Pinho Ferreira, W. Tillmann, Experimental and statistical analysis of the wear of diamond impregnated tools, *Wear.* 2020, p. 203574, <https://doi.org/10.1016/j.wear.2020.203574>.
- [21] S. Tan, W. Zhang, L. Duan, B. Pan, M. Rabiei, C. Li, Effects of MoS<sub>2</sub> and WS<sub>2</sub> on the matrix performance of WC based impregnated diamond bit, *Tribol. Int.* 131 (2019) 174–183, <https://doi.org/10.1016/j.triboint.2018.10.038>.
- [22] H. Chang, P. Borghesani, Z. Peng, Automated assessment of gear wear mechanism and severity using mould images and convolutional neural networks, *Tribol. Int.* 147 (2020) 106280, <https://doi.org/10.1016/j.triboint.2020.106280>.
- [23] S. Wang, T.H. Wu, T. Shao, Z.X. Peng, Integrated model of BP neural network and CNN algorithm for automatic wear debris classification, *Wear.* 426–427 (2019) 1761–1770, <https://doi.org/10.1016/j.wear.2018.12.087>.
- [24] S. Perez, M. Karakus, F. Pellet, Development of a tool condition monitoring system for impregnated diamond bits in rock drilling applications, *Rock Mech. Rock. Eng.* 50 (2017) 1289–1301, <https://doi.org/10.1007/s00603-016-1150-6>.
- [25] M. Karakus, S. Perez, Acoustic emission analysis for rock-bit interactions in impregnated diamond core drilling, *Int. J. Rock Mech. Min. Sci.* 68 (2014) 36–43, <https://doi.org/10.1016/j.ijrmms.2014.02.009>.
- [26] K. He, G. Gkioxari, P. Dollár, R. Girshick, Mask R-CNN, in: 2017 IEEE Int. Conf. Comput. Vis. ICCV, 2017, pp. 2980–2988, <https://doi.org/10.1109/ICCV.2017.322>.
- [27] B. Kim, S. Cho, Image-based concrete crack assessment using mask and region-based convolutional neural network, *Struct. Control. Health Monit.* 26 (2019), e2381, <https://doi.org/10.1002/stc.2381>.
- [28] F. Wei, G. Yao, Y. Yang, Y. Sun, Instance-level recognition and quantification for concrete surface bughole based on deep learning, *Autom. Constr.* 107 (2019), <https://doi.org/10.1016/j.autcon.2019.102920>.
- [29] S. Masubuchi, E. Watanabe, Y. Seo, S. Okazaki, T. Sasagawa, K. Watanabe, T. Taniguchi, T. Machida, Deep-learning-based image segmentation integrated with optical microscopy for automatically searching for two-dimensional materials, *Npj 2D Mater. Appl.* 4 (2020) 1–9, <https://doi.org/10.1038/s41699-020-0137-z>.
- [30] M. Frei, F.E. Kruis, FibreR-CNN: expanding Mask R-CNN to improve image-based fiber analysis, *Powder Technol.* 377 (2021) 974–991, <https://doi.org/10.1016/j.powtec.2020.08.034>.
- [31] X. Liu, D. Zhao, W. Jia, W. Ji, C. Ruan, Y. Sun, Cucumber fruits detection in greenhouses based on instance segmentation, *IEEE Access.* 7 (2019) 139635–139642, <https://doi.org/10.1109/ACCESS.2019.2942144>.
- [32] L. Costa, L. Archer, Y. Ampatzidis, L. Casteluci, G.A.P. Caurin, U. Albrecht, Determining leaf stomatal properties in citrus trees utilizing machine vision and artificial intelligence, *Precis. Agric.* (2020), <https://doi.org/10.1007/s11119-020-0971-x>.
- [33] Y. Liu, P. Zhang, Q. Song, A. Li, P. Zhang, Z. Gui, Automatic segmentation of cervical nuclei based on deep learning and a conditional random field, *IEEE Access.* 6 (2018) 53709–53721, <https://doi.org/10.1109/ACCESS.2018.2871153>.
- [34] K. Long, L. Tang, X. Pu, Y. Ren, M. Zheng, L. Gao, C. Song, S. Han, M. Zhou, F. Deng, Probability-based Mask R-CNN for pulmonary embolism detection, *Neurocomputing.* 422 (2021) 345–353, <https://doi.org/10.1016/j.neucom.2020.10.022>.
- [35] H. Kim, J. Han, T.Y.-J. Han, Machine vision-driven automatic recognition of particle size and morphology in SEM images, *Nanoscale.* 12 (2020) 19461–19469, <https://doi.org/10.1039/DONR04140H>.
- [36] Z. Chen, X. Liu, J. Yang, E. Little, Y. Zhou, Deep learning-based method for SEM image segmentation in mineral characterization, an example from Duvernay Shale samples in Western Canada Sedimentary Basin, *Comput. Geosci.* 138 (2020) 104450, <https://doi.org/10.1016/j.cageo.2020.104450>.
- [37] facebookresearch/detectron2, <https://github.com/facebookresearch/detectron2>, 2021 (accessed February 21, 2021).
- [38] S. Tan, C. Li, X. Fang, H. Shi, L. Duan, C. Li, Investigation of filling phase percentages on the performance of WC-cu based hot-pressing diamond bit matrices, *Metals.* 9 (2019) 1305, <https://doi.org/10.3390/met9121305>.
- [39] S. Wen, P. Huang, Principles of Tribology, John Wiley & Sons Singapore Pte. Ltd., Singapore, 2017, <https://doi.org/10.1002/9781119214908>.
- [40] R. Girshick, J. Donahue, T. Darrell, J. Malik, Rich feature hierarchies for accurate object detection and semantic segmentation, in: 2014 IEEE Conf. Comput. Vis. Pattern Recognit, 2014, pp. 580–587, <https://doi.org/10.1109/CVPR.2014.81>.
- [41] R. Girshick, Fast R-CNN, in: 2015 IEEE Int. Conf. Comput. Vis. ICCV, 2015, pp. 1440–1448, <https://doi.org/10.1109/ICCV.2015.169>.
- [42] S. Ren, K. He, R. Girshick, J. Sun, Faster R-CNN: towards real-time object detection with region proposal networks, *IEEE Trans. Pattern Anal. Mach. Intell.* 39 (2017) 1137–1149, <https://doi.org/10.1109/TPAMI.2016.2577031>.
- [43] M. Frei, F.E. Kruis, Image-based size analysis of agglomerated and partially sintered particles via convolutional neural networks, *Powder Technol.* 360 (2020) 324–336, <https://doi.org/10.1016/j.powtec.2019.10.020>.

---

## PRODUCTION, STRUCTURE, PROPERTIES

---

# D-Optimal Mixture Design of Fe-Based Pre-Alloyed Diamond Bit Matrix with Low Liquid Phase Content

**Zhiming Wang<sup>a</sup>, Xiaohong Fang<sup>a</sup>, \*, Wucheng Sun<sup>a</sup>, Longchen Duan<sup>a</sup>, and Songcheng Tan<sup>a</sup>**

<sup>a</sup> Faculty of Engineering, China University of Geosciences, Wuhan, 430074 China

\*e-mail: duyaoff@163.com

Received September 29, 2020; revised October 12, 2020; accepted October 28, 2020

**Abstract**—To explore a new formulation system of diamond bit matrix, three kinds of Fe-based pre-alloyed powder with low liquid phase content were utilized for the matrix fabrication of impregnated diamond bit (IDB). To this end, the D-optimal mixture design method was employed for the design of the experiment scheme which contained 16 groups of samples. The samples were fabricated under the same hot pressing sintering conditions, then tests on hardness, bending strength, and relative density were conducted. The results were analyzed by regression analysis, and so were the interrelations and interactions of formula components on matrix properties. Meanwhile, the fracture surface of samples after the bending strength test was observed by SEM. It was found that FAM1020 and FAM2120 have a positive effect on the bending strength of metal matrix composite. Besides, FAM2120 has a positive effect on the hardness of the matrix, but a negative effect on the bending strength of the diamond matrix composite. The interaction among the three powders can improve the performance of the matrix. According to the result, the Fe-based pre-alloyed bit matrix with low liquid phase content can meet the requirements of the diamond bit matrix. Based on this exploration experiment, an optimal formulation is concluded as 50 wt %  $X_1$ , 30 wt %  $X_2$ , 20 wt %  $X_3$ .

**Keywords:** D-optimal mixture design, regression analysis, impregnated diamond bit, iron-based, low liquid phase content

**DOI:** 10.3103/S1063457621040080

## INTRODUCTION

The energy and mineral resources exploration and development is an important pillar to support a country's economic development [1]. With the rapid development of social economy, there is an increasing demand for various underground mineral resources in the market [2]. As an efficient drilling method in hard rock, impregnated diamond bit (IDB) drilling is widely applied in geological drilling industry [3, 4]. The matrix of the diamond bit, one of the key factors to ensure the quality of the bit, is to locate the diamond and to provide a combination with the diamond [5]. More importantly, the metal matrix composite (MMC) should not only wrap the diamond up firmly but also need to be worn continuously during the drilling process to ensure that the diamond can be continuously sharpened [6].

In the traditional industry of diamond bit manufacturing, the bit matrix includes the WC-based, Co-based, and Cu-based mixed powders [7, 8]. Due to the strategic value and rising price of the raw materials, a new system of the matrix materials has been a research hotspot for scholars recently. To acquire a good drilling effect in hard and compact rock, grinding aids were added in the diamond contained layer to develop a kind of diamond bit [9]. High-temperature solid lubricants are a new approach to improve the performance of Fe-based IDB. To figure out their influences on the performance of the matrix composites, some solid lubricants ( $\text{CaF}_2$ , hBN, graphite) were doped into the matrix of the drill bit as an additive [10, 11]. It is believed that with the decrease of graphite particle size, the bending strength and friction coefficient of the matrix gradually decreased, while the hardness of the matrix and service life of the working layer increased gradually.

In [12–21], the state of research in the field of sintering of composite diamond-containing materials based on metal and carbide matrices used for the manufacture of drilling and cutting tools is analyzed. The positive effect of additions of  $\text{CrB}_2$  powder [22, 23] and nanodispersed VN powder [24–27] on the microstructure, mechanical and tribological properties of such composites is known. At that, the grain size in the sintered composite can decrease and the phase composition can be homogenized. In this case, a sig-

nificant improvement in mechanical and tribological properties occurs in the composite [25–27]. To optimize and predict the tribological characteristics of composite diamond-containing materials, it is necessary to take into account that, during operation, their wear resistance is influenced by the developed contact loads [28–30] and temperatures [31–33], as well as the “degree” of equipping the working surface of the tool with composite materials [34]. All this causes intense wear of the matrix material [20–25] and imposes high requirements on the mechanical and tribological characteristics of composite diamond-containing materials.

To reduce the cobalt content in the matrix, iron, which belongs to the VIII family of transition metals just like cobalt, was used to explore a new matrix system [35, 36]. In this case, a large number of studies on iron-based composites have emerged [37, 38]. What's more, the pre-alloyed powders can obtain better performance than the elemental powder of the hot pressed sintering process [39–41]. As an example, a series of Fe–Co–Cu pre-alloyed powder bits were developed and tested with the result that the 65% Fe–20% Cu–15% Co alloy had the optimal performance for application in IDBs [42].

As shown in the above mentioned research, it is obviously that diamond matrix is composed of a variety of materials. For a new formulation system of the diamond matrix, a lot of experimental research is needed to verify its feasibility and the effect of various material parts on matrix performance. Therefore, a reasonable experimental design method is particularly important to develop the new formulation system of the diamond matrix in the early stage.

Mixture design experiment is a common experimental design method which can reduce the number of experiments and evaluate many factors and their effects [43, 44]. The regression equations of the components and the responses should be obtained by the mixture experiments of different percentages of components [45–47]. Finally, statistical conclusions are drawn from the regression equation and its graph response surface plot [48]. In the experimental design, the percentage of each powder must add up to 1, which means that these components X, mixing factors, cannot be completely independent of one another with their ratio must lie between 0 and 1 [49]. Therefore, data analysis becomes more challenging because the mixing factors are interrelated, whereas the D-optimal mixture design (DMD) provides an effective method to accordingly change the mix composition and explore how this change will affect the performance of the mixed material [50]. At present, the D-optimal mix design has been widely applied in pharmaceutical, food, and concrete mix design, which can significantly reduce the workload of this stage of the test and improve the efficiency of the test [51, 52]. Likewise, D-optimal mixture design should be an effective experimental design method to develop a new formulation system of IDB in its early stage.

Based on this, a Fe-based pre-alloyed matrix system with low liquid phase content was studied by D-optimal mixture design. Three kinds of Fe-based pre-alloyed powders with low liquid phase content were selected to figure out the effect law of these three kinds of powders on matrix hardness, bending strength, and bending strength loss rate, which can provide a reference for the research on Fe-based drill bits with low liquid phase content.

## 2. EXPERIMENTAL

### 2.1. Materials

Three Fe based pre-alloyed powders, FAM1020 (Fe–Ni18%–Co2%, average particle size 38 μm), FAM2120 (Fe–Ni6%–Cu6%–Sn3%, average particle size 36 μm) and FAM3010 (Fe–Ni7%–Mn12%, average particle size 29 μm), were provided by Forlong Advanced materials company in Hunan Province, China. This hot pressing sintering process is termed low-liquid phase sintering because the contents of low melting point metals Cu and Sn in the three Fe-based pre-alloys powders are extremely low compared with the conventional diamond bit formulation system.

### 2.2. Experimental Design

A 16-run, three-factor, five-response D-optimal mixture design was employed in this study to research the performance variations of the Fe-based bit matrix with low liquid phase content. The factors evaluated in the study were the mass fraction of pre-alloyed powder FAM1020 ( $X_1$ ), FAM2120 ( $X_2$ ), FAM3010 ( $X_3$ ). In the experimental applications, however, it is unrealistic to allow the mixture constituent to vary between 0 and 1. Instead, a more realistic approach is to set limits on the composition to limit the range of variation of a component. According to the preliminary experiment, the proportion of the above three materials is  $20 \leq X_1 \leq 60$  wt %,  $10 \leq X_2 \leq 50$  wt %,  $20 \leq X_3 \leq 40$  wt %, and the sum of the three factors should be equal to 100%. The response value  $Y$  is the hardness ( $Y_1$ ), bending strength ( $Y_2$ ) of metal matrix composite

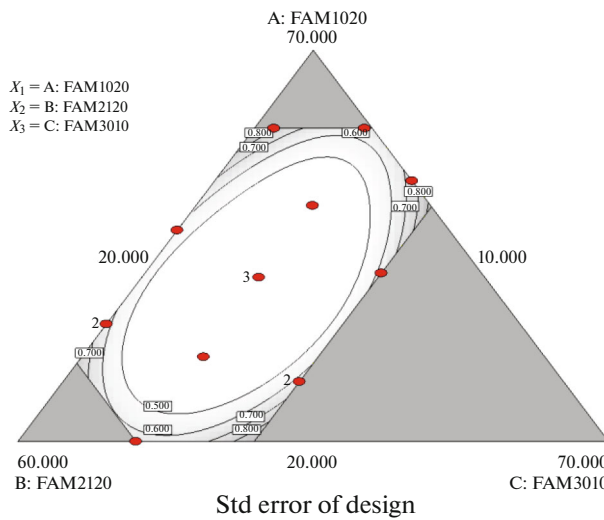


**Fig. 1.** Schematic representation of the three-component D-optimal mixture design.

(MMC), bending strength ( $Y_3$ ) of diamond matrix composite (DMC), bending strength loss rate ( $Y_4$ ), and relative density ( $Y_5$ ) of the bit matrix.

The experimental design scheme was generated by Design-Expert software. Mixture design is to reasonably select a small number of experimental points. These points included factorial points, centers of edges, centers of the constraint plane, axial checkpoints, and overall center point, as shown in Fig. 1. Geometrically, this is equivalent to laying out the edges of the mixture so that the experimental area can be mapped as much as possible. This kind of design largely depends on the selected polynomial model. Under the constraint conditions, 16 formulations were generated as shown in Table 1.

**Table 1.** Formulations of Fe based pre-alloyed matrix with low liquid phase content

Formulation	Mass fraction, wt %			Element content, wt %					
	FAM1020	FAM2120	FAM3010	Fe	Ni	Co	Cu	Sn	Mn
1	41	29	30	81.75	11.22	0.82	1.74	0.87	3.6
2	50	20	30	81.3	12.3	1	1.2	0.6	3.6
3	42	18	40	81.3	11.44	0.84	1.08	0.54	4.8
4	20	50	30	82.8	8.7	0.4	3	1.5	3.6
5	31	39	30	82.25	10.02	0.62	2.34	1.17	3.6
6	35	45	20	82.45	10.4	0.7	2.7	1.35	2.4
7	28	32	40	82	9.76	0.56	1.92	0.96	4.8
8	41	29	30	81.75	11.22	0.82	1.74	0.87	3.6
9	41	29	30	81.75	11.22	0.82	1.74	0.87	3.6
10	60	11	29	80.84	13.49	1.2	0.66	0.33	3.48
11	28	32	40	82	9.76	0.56	1.92	0.96	4.8
12	20	50	30	82.8	8.7	0.4	3	1.5	3.6
13	60	18	22	81.12	13.42	1.2	1.08	0.54	2.64
14	53	10	37	80.87	12.73	1.06	0.6	0.3	4.44
15	47	33	20	81.85	11.84	0.94	1.98	0.99	2.4
16	35	45	20	82.45	10.4	0.7	2.7	1.35	2.4

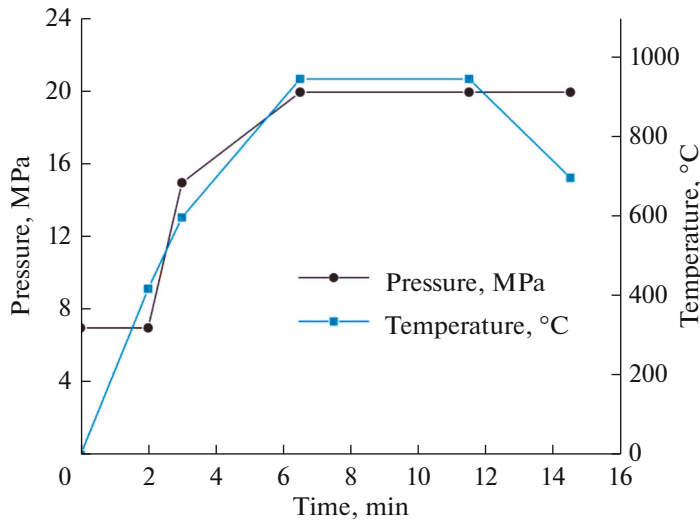


**Fig. 2.** The curves of sintering process of bit matrix.

### 2.3. Samples Preparation and Test

Three kinds of pre-alloyed powders, with formula number 17 (100 wt % FAM1020), 18 (100 wt % FAM2120), 19 (100 wt % FAM3100), were fabricated by hot pressing sintering and tested for comparison. All specimens were divided into two groups, i.e., diamond-containing group and diamond-free group, both of which included two samples respectively in each powder formulation, and the dimension of specimens was  $30 \times 5 \times 5$  mm. In the preparation of DMC, the diamond concentration of DMC samples was 25 vol %, with an average particle size of 250 to 270  $\mu\text{m}$ , i.e., 50 to 60 meshes. The powder mixtures were separately mixed in a ball mill for 8 h, which were later sent into a controlled resistor furnace (SM-100E) for hot-pressed sintering. The sintering parameters are shown in Fig. 2.

The Rockwell hardness and the bending strength were then measured by a Rockwell hardness tester (HR-150A, Shandong Yexian Testing Machine Factory, Jinan, Shandong, China) and a PC controlled universal testing machine (CTM2500, Shanghai Xieqiang Instrument Technology Co., Ltd., Shanghai, China) respectively. The Archimedes method was used to measure the relative density of metal matrix composite (MMC). Furthermore, the fracture surface of different formula specimens after the bending strength test was observed by SEM (phenom G2). In this manner, the grain size, pore size, and number in the fracture micromorphology were observed to analyze the effect law of different content of components on the performance of the matrix. Meanwhile, the regression analysis of variance was used to analyze the influence of the response value on matrix performance.

## 3. RESULTS AND DISCUSSION

### 3.1. Experimental Results

The experimental results are given in Table 2. To refrain from the deviation, the data obtained in the experiment were taken as the average value. Besides, the statistical significance of the data was evaluated using Student's *t*-test and  $P < 0.05$  or 0.01 is taken as significant. To fit the data, different polynomial models were matched to describe the correlation between the response value and the variable. In this manner, the Quadratic model and the Special Cubic model were applied to fit  $Y_1$ ,  $Y_3$ , respectively, both  $Y_2$  and  $Y_4$  are Cubic models. As for the relative density  $Y_5$ , in this study, it was not analyzed with the reason that the value of  $Y_5$  is mainly related to sintering factors, rather than the changes in matrix composition.

### 3.2. Regression Analysis

**3.2.1. Rockwell hardness ( $Y_1$ ).** The Rockwell hardness values of Fe-based pre-alloyed bit matrix with low liquid phase content are between 90 and 110. The regression equation from the results in Table 2 is presented as follows:

$$Y_1 = 0.2498X_1 + 0.3813X_2 - 1.2746X_3 + 0.01595X_1X_2 + 0.04988X_1X_3 + 0.04463X_2X_3. \quad (1)$$

**Table 2.** Measured responses value for the three-component D-optimal mixture design

Random order	FAM1020, wt %	FAM2120, wt %	FAM3010, wt %	$Y_1$ , HRB	$Y_2$ , MPa	$Y_3$ , MPa	$Y_4$	$Y_5$
1	41	29	30	102.5	925	455	0.508	0.943
2	50	20	30	101.9	895	415	0.536	0.954
3	42	18	40	96.3	835	430	0.485	0.909
4	20	50	30	102	848	375	0.579	0.921
5	31	39	30	96.3	915	407.5	0.555	0.919
6	35	45	20	99.5	905	392.5	0.566	0.928
7	28	32	40	94.2	780	425	0.455	0.940
8	41	29	30	103.6	905	417.5	0.539	0.945
9	41	29	30	103	885	410	0.537	0.948
10	60	11	29	91.5	912.5	390	0.573	0.919
11	28	32	40	95.3	770	410	0.468	0.938
12	20	50	30	98.7	812.5	337.5	0.585	0.920
13	60	18	22	94.5	1007.5	412.5	0.591	0.908
14	53	10	37	92.1	982.5	480	0.511	0.922
15	47	33	20	101.3	865	482.5	0.442	0.931
16	35	45	20	100.2	905	389	0.570	0.926
17	100	0	0	89.7	822.5	445	0.459	0.912
18	0	100	0	94.4	770	217.5	0.718	0.926
19	0	0	100	88.3	720	410	0.431	0.906

With R-square = 0.72, adj R-square = 0.58, adeq precision = 5.941.

Analysis of variance (ANOVA) for  $Y_1$  are given in Table 3. Above all, “Adeq Precision” measures the signal to noise ratio and a ratio greater than 4 is desirable. The “Adeq Precision” of 5.941 indicates an adequate signal that the model can be used to navigate the design space, as well as the Model F-value of 5.16, which implies the model is significant. Values of “Prob > F” less than 0.0500 indicate model terms are significant. In this case, Linear Mixture Components,  $X_1X_2$ ,  $X_1X_3$ ,  $X_2X_3$  are significant model terms. Besides, values greater than 0.1000 indicate the model terms are not significant. If there are many insignificant model terms (not counting those required to support hierarchy), model reduction may improve your model. The effect of  $X_3$  on hardness is the most significant although it is negative. For another, it could be seen from equation (1) that the positive effect on hardness of  $X_2$  is the most significant, which is consistent with the results of comparative experiments that formula 18 with 100% wt FAM2120 had the highest hardness value. Combined with Fig. 3, it could be seen that the interaction between the three pre-alloyed powders is obvious. The profile of the response surface plot is convex, which means that the interaction between the three powders had a significant effect on  $Y_1$ . To maintain a high hardness, an approximate range can be obtained from the diagram i.e.,  $35 \leq X_1 \leq 50$  wt %,  $30 \leq X_2 \leq 50$  wt %.

**3.2.2. Bending strength ( $Y_2$ ) of MMC and bending strength loss rate ( $Y_4$ ).** The cubic model was recommended for response  $Y_2$  and  $Y_4$  with the reason that it's the optimal model for the experimental result.  $Y_2$  is the bending strength of MMC and  $Y_4$  is the loss rate of bending strength of the matrix obtained by formula (2).

$$SLR = \frac{Y_2 - Y_3}{Y_2} \times 100\%. \quad (2)$$

The following cubic equations were used to demonstrate the relationship between the formulation compositions  $X_1$ ,  $X_2$ ,  $X_3$ , and the responses  $Y_2$  and  $Y_4$ .

$$Y_2 = 303.195X_1 + 281.319X_2 - 2765.517X_3 - 3.73625X_1X_2 + 47.29622X_1X_3 + 46.82317X_2X_3 - 0.71795X_1X_2X_3 - 3.0613 \times 10^{-3}X_1X_2(X_1 - X_2) - 0.43529X_1X_3(X_1 - X_3) - 0.41253X_2X_3(X_2 - X_3). \quad (3)$$

**Table 3.** Analysis of variance (ANOVA) for regression model  $Y_1$ 

Source	Sum of squares	Degree of freedom	Mean square	F-value	P-value Prob > F
Model	174.10	5	34.82	5.16	0.0134
Linear mixture	71.66	2	35.83	5.31	0.0269
$X_1X_2$	76.14	1	76.14	11.28	0.0073
$X_1X_3$	63.19	1	63.19	9.36	0.0121
$X_2X_3$	54.00	1	54.00	8.00	0.0179
Residual	67.51	10	6.75		
Cor total	241.61	15			

With R-square = 0.97, adj R-square = 0.94, adeq precision = 18.123.

$$Y_4 = 0.13187X_1 + 0.16275X_2 - 1.04278X_3 - 2.95901 \times 10^{-3} X_1X_2 + 0.017383X_1X_3 + 0.016337X_2X_3 \\ - 2.32634 \times 10^{-4} X_1X_2X_3 - 6.07387 \times 10^{-7} X_1X_2(X_1 - X_2) - 1.64303 \times 10^{-4} X_1X_3(X_1 - X_3) \\ - 1.63665 \times 10^{-4} X_2X_3(X_2 - X_3). \quad (4)$$

With R-squared = 0.98, adj R-squared = 0.95, adeq precision = 17.291.

Particularly, the R-square of the two models is greater than 0.97 and the adeq precision is far greater than 4, both of which mean that the model is significant. Choosing  $Y_2$  for analysis of variance, the  $p$ -value of the model in Table 4 is far less than 0.0500, indicating that the model is significant. Equation (3) indicates that FAM1020 ( $X_1$ ), FAM2120 ( $X_2$ ) had a positive effect on the bending strength of MMC, while FAM 3100 ( $X_3$ ) had a negative effect. However, the interaction between  $X_3$  and  $X_1$ ,  $X_2$  also makes a difference in the  $Y_2$ . It can be seen from Fig. 4 that FAM3010 has a significant effect on  $Y_2$ . To get an applicable value of  $Y_2$ , a narrowed scale of  $X_3$ ,  $20 \leq X_3 \leq 23$  wt % or  $32 \leq X_3 \leq 37$  wt %, was concluded by regression analysis and Fig. 4.

**3.2.3. Bending strength ( $Y_3$ ) of DMC.** The bending strength of the diamond matrix composite is  $Y_3$ . The polynomial was obtained by fitting the experimental results, and shown as follows:

$$Y_3 = -14.47366X_1 - 33.86014X_2 - 20.85507X_3 + 1.32346X_1X_2 + 0.958517X_1X_3 + 1.5111X_2X_3 \\ - 0.040408X_1X_2X_3. \quad (5)$$

With R-square = 0.88, adj R-square = 0.81, adeq precision = 12.415.

It can be seen from the equation (5) that FAM2120 ( $X_2$ ) has a greater negative effect on the bending strength of diamond matrix samples, which can also be verified by the value of the formula no. 18. According to ANOVA given in Table 5, the Model F-value of 11.46 implies that the model is significant, in the meantime, the values of “Prob > F” less than 0.0500 indicate that the model terms are significant.  $P$ -val-

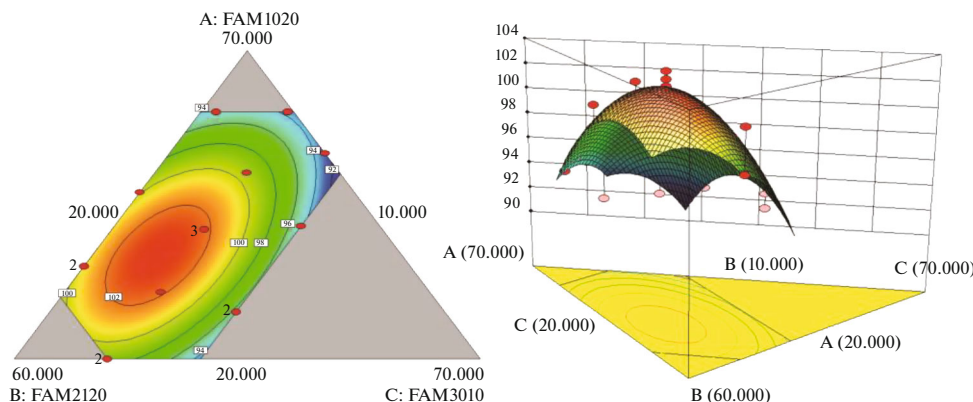


**Fig. 3.** Contour plot and response surface plot showing the effect of the amount of FAM1020 ( $X_1$ ), FAM2120 ( $X_2$ ), and FAM3010 ( $X_3$ ) on the response  $Y_1$ .

**Table 4.** Analysis of variance (ANOVA) for regression model  $Y_2$ 

Source	Sum of squares	Degree of freedom	Mean square	F-value	P-value Prob > F
Model	61259.64	9	6806.63	25.92	0.0004
Linear mixture	38805.64	2	19402.82	73.90	<0.0001
$X_1X_2$	8198.00	1	8198.00	31.22	0.0014
$X_1X_3$	8252.03	1	8252.03	31.43	0.0014
$X_2X_3$	9082.88	1	8082.88	30.78	0.0014
$X_1X_2X_3$	7791.73	1	7791.73	29.68	0.0016
$X_1X_2(X_1 - X_2)$	460.29	1	460.29	1.75	0.2337
$X_1X_3(X_1 - X_3)$	8888.74	1	8888.74	33.85	0.0011
$X_2X_3(X_2 - X_3)$	7387.96	1	7387.96	28.14	0.0018
Residual	1575.36	6	262.56		
Cor total	62835.00	15			

ues show the interactions between  $X_1$  and  $X_2$ ,  $X_2$  and  $X_3$ ,  $X_1$  and  $X_3$ ,  $X_1$ ,  $X_2$  and  $X_3$ , which are significant at  $P < 0.001$ ,  $P < 0.05$ ,  $P < 0.05$  and  $P < 0.01$ , respectively. Similarly, it can be seen in Fig. 5 that the three pre-alloyed powders with different contents have complex interaction effects. Overall, the higher the content of FAM2120, the lower that of  $Y_3$ . Considering the interaction between the three materials, a better range can be obtained from Fig. 5, i.e.,  $35 \leq X_1 \leq 55$  wt %,  $20 \leq X_2 \leq 40$  wt %.

The calculated values and experimental values of all regression models are shown in Fig. 6, from which we can see that the model results are in good agreement with the experimental data. In general, some conclusions can be concluded through the regression analysis of experimental data. FAM2120 has a positive effect on the Rockwell hardness of the matrix, on the other hand, more content of FAM1020 means higher bending strength of the MMC. Furthermore, FAM2120 has a negative effect on the bending strength of the DMC. The strength values of formula 4 and formula 12 with a 50 wt % content of FAM2120 in both formulations are the lowest in Fig. 6c, indicating that a high content of FAM2120 drags down the holding force of the matrix. When the content of FAM3100 is low, the matrix has better mechanical properties, which can be used as an additive to adjust the performance of the matrix. Finally, considering that all responses need to maintain a suitable range of the bit matrix, a better range of experimental materials can be derived from all the analyses i.e.,  $35 \leq X_1 \leq 55$  wt %,  $20 \leq X_2 \leq 45$  wt %,  $25 \leq X_3 \leq 35$  wt %.

### 3.3. Fracture Micromorphology Analysis

The micromorphology of the matrix sample after the bending test is shown in Fig. 7. The content of FAM3100 is 30 wt % in formula 2, 4, 9, and the sequence of content for FAM1020 is no. 2 > no. 9 > no.

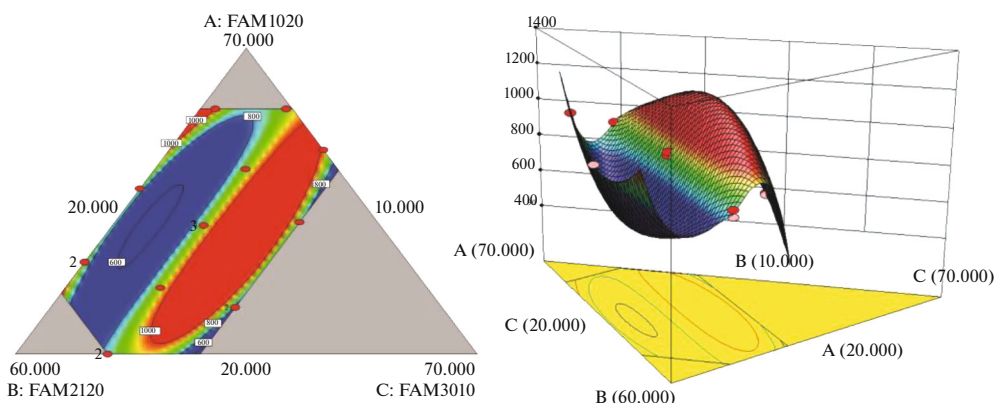


**Fig. 4.** Contour plot and response surface plot showing the effect of the amount of FAM1020 ( $X_1$ ), FAM2120 ( $X_2$ ), and FAM3010 ( $X_3$ ) on the response  $Y_2$ .

**Table 5.** Analysis of variance (ANOVA) for regression model  $Y_3$ 

Source	Sum of squares	Degree of freedom	Mean square	F-value	P-value Prob > F
Model	19410.32	6	3235.05	11.46	0.0009
Linear mixture	7393.52	2	3696.76	13.10	0.0022
$X_1X_2$	8033.80	1	8033.80	28.47	0.0005
$X_1X_3$	2774.19	1	2774.19	9.83	0.0120
$X_2X_3$	2972.40	1	2972.40	10.53	0.0101
$X_1X_2X_3$	5201.92	1	5201.92	18.43	0.0020
Residual	2539.61	9	282.18		
Cor total	21949.94	15			

4. As for the matrix without diamond, both  $X_1$  and  $X_2$  have a positive effect on the bending strength except  $X_3$ , the degree of influence on  $Y_2$  of MMC is  $X_1 > X_2$ . Some micro crevices can be observed in Fig. 7b, which can be attributed to the highest content of FAM2120 in formula 4. As shown in Figs. 7a, 7b, 7c), it can be seen that the fracture surface of formula 2 is the densest because of the minimum content of FAM2120 and the highest content of FAM1020. To further verify the results of regression analysis, the fracture surface of formulas 17, 18, and 19 are shown in Figs. 7d, 7e, 7f, respectively. The fracture surface of formula 17 has the best homogeneity, and crystal boundary can be observed from Fig. 7e. The three kinds of pre-powders have different microscopic characteristics after sintering, therefore, when the three pre-powders are mixed in a certain proportion, the interaction between the two components and even among the three components has a great impact on the mechanical properties of the matrix.

The morphologies of the fracture surface of the DMC and diamond-metal matrix interface of the above the six formulas are shown in Fig. 8. In Fig. 8a, the diamond-metal matrix is uniform with few pores, which indicates that the diamond matrix is firmly in contact with the diamond. The pores in the diamond-metal matrix of formula 4 in Fig. 8b are significantly increased, while the number of pores in the formula 9 is between the formula 2 and formula 4. Analysing the composition of the formulations, it can be seen that there is the highest content of FAM2120 in formula 4, which is consistent with the negative effect of FAM2120 on  $Y_2$  in regression analysis. Theoretically, the existence of the liquid phase Cu and Sn in the matrix will fill the micro crevices during the sintering process, which will enhance the mechanical properties of the matrix. However, compared with the conventional Fe-based bit matrix system, this content of the liquid phase can be ignored. Moreover, the grain boundary of the FAM2120 matrix in Fig. 7e is visible. When the fracture occurs, the fracture is easy to propagate along the grain boundary, which results in the Low bending strength. The results show that with the increase of FAM2120 content, the bending strength of DMC decreases, which is consistent with the results of regression analysis.

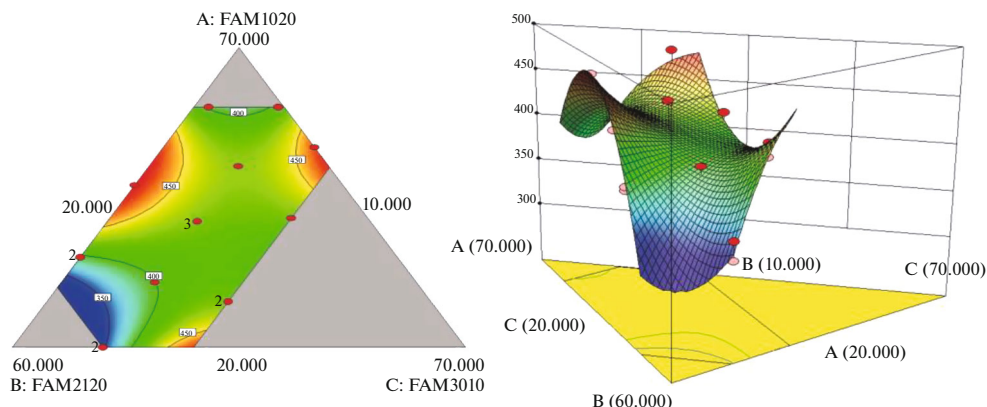


**Fig. 5.** Contour plot and response surface plot showing the effect of the amount of FAM1020 ( $X_1$ ), FAM2120 ( $X_2$ ), and FAM3010 ( $X_3$ ) on the response  $Y_3$ .

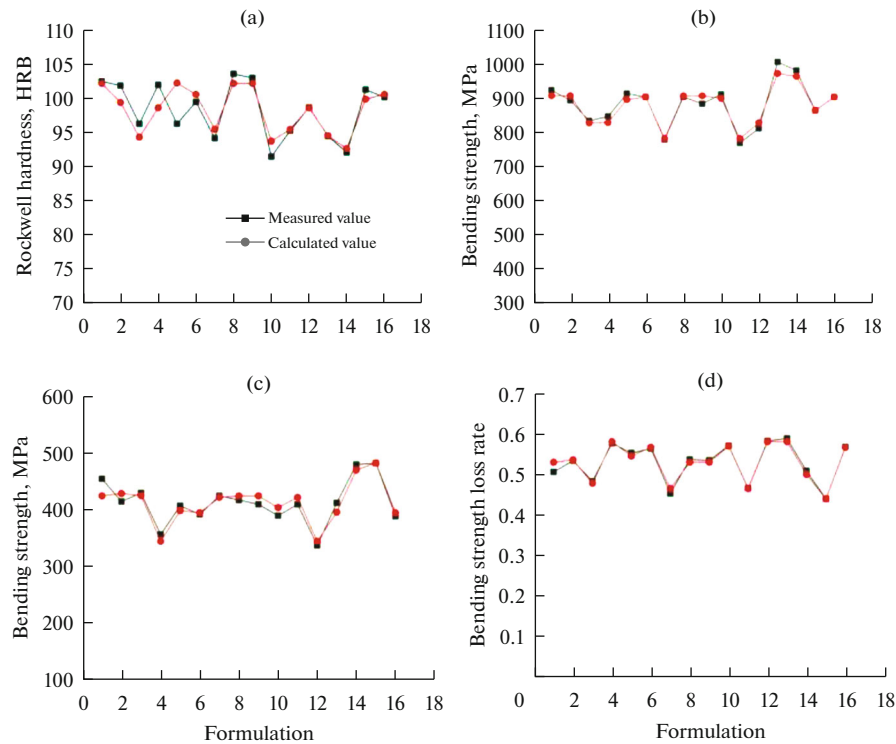


**Fig. 6.** Fitting effect of the regression equation. (a) Rockwell hardness, (b) bending strength of MMC, (c) bending strength of DMC, (d) bending strength loss rate.

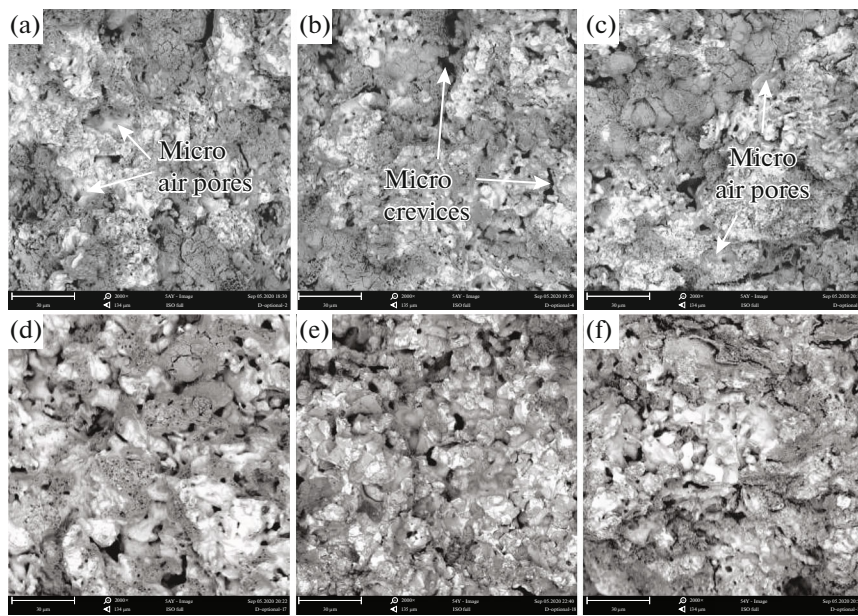


**Fig. 7.** Fracture surfaces of MMC samples after bending strength (2000 $\times$ ); (a) formula no. 2; (b) formula no. 4; (c) formula no. 9; (d) formula no. 17; (e) formula no. 18; (f) formula no. 19.

### 3.4. Optimization of the Matrix Formulation

After obtaining the regression equations, optimization on the formulation was carried out to obtain the content values of  $X_1 - X_3$ , maximizing the responses ( $Y_1 - Y_4$ ) simultaneously. These constraints were made to obtain a matrix formulation with excellent performance. The optimized content values (50 wt %  $X_1$ , 30 wt %  $X_2$ , 20 wt %  $X_3$ ) of the matrix formulation and the predicted responses ( $Y_1 - Y_4$ ) are given in

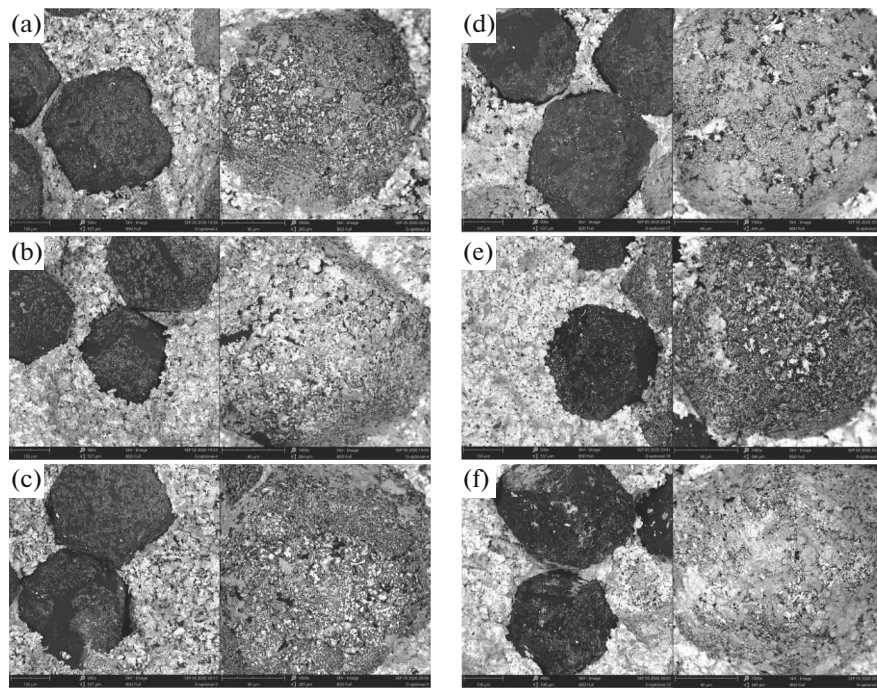


**Fig. 8.** Morphologies of the fracture surfaces ( $500\times$ ) and diamond-metal matrix interfaces ( $1000\times$ ) of the DRC samples after bending strength; (a) formula no. 2; (b) formula no. 4; (c) formula no. 9; (d) formula no. 17; (e) formula no. 18; (f) formula no. 19.

**Table 6.** Predicted and measured values of the responses

	$X_1$ , wt %	$X_2$ , wt %	$X_3$ , wt %	$Y_1$ , HRB	$Y_2$ , MPa	$Y_3$ , MPa	$Y_4$	$Y_5$	Desirability
Predicted value	50	30	20	99	910.5	481.5	0.471		0.755
Measured value				97.5	1010	545	0.460	0.946	

Table 6. To verify the responses, the optimal formulation was prepared to fabricate the samples. In the previous regression analysis, the range of material content with excellent response values was obtained, while the optimal formula was included. The measured values presented in Table 6 are close to the predicted values, with a range of 1.5 to 11.7% in relative errors.

#### 4. CONCLUSIONS

The experimental study on the Fe-based bit matrix with low liquid phase content was carried out by D-optimal mixture design. Combined with the microscopic characteristics of the fracture surface, the experimental results were analyzed by regression analysis and some conclusions could be obtained as follows:

- (1) The application of the D-optimal mixture design method in the design of the formula in IDB is effective and reliable. From the data results, the Fe-based pre-alloyed bit matrix with low liquid phase content can meet the requirements of the bit matrix.
- (2) According to the regression analysis, the three kinds of Fe-based pre-alloyed powders have different properties, and the interaction among them can improve the performance of the matrix.
- (3) FAM1020 and FAM2120 have a positive effect on the bending strength of MMC. Besides, FAM2120 has a positive effect on the hardness of the matrix, but a negative effect on the bending strength of the DMC. When the content value of FAM3100 is low than 23 wt % or between  $32 \leq X_3 \leq 37$  wt %, it has a better effect on the performance of the matrix.

(4) In the case where the Rockwell hardness along with the bending strength of MMC and DMC reach the highest comprehensive values while the samples achieve the lowest bending strength loss rate, there comes out the optimal formulation with 50 wt %  $X_1$ , 30 wt %  $X_2$ , 20 wt %  $X_3$ .

## FUNDING

This study was financially supported by the National Natural Science Foundation of China (grant nos. 41972327 and 41672364), External Cooperation Program of Science and Technology Department of Hubei Province (2019AHB051), the open project of Engineering Research Center of Rock-Soil Drilling & Excavation and Protection (grant no. 201907), and the experimental technology research project, China University of Geosciences, Wuhan (grant no. SJ-201708).

## CONFLICT OF INTEREST

The authors declare that they have no conflicts of interest.

## REFERENCES

1. Zhao, X.J., Li, J.Y., Duan, L.C., Tan, S.C., and Fang, X.H., Effect of Fe-based pre-alloyed powder on the microstructure and holding strength of impregnated diamond bit matrix, *Int. J. Refract. Met. Hard Mater.*, 2019, vol. 79, pp. 115–122.
2. Li, S.B., Xiang, Q., and Zhang, L.G., The wear mechanisms of diamond impregnated bit matrix, *Appl. Mech. Mater.*, 2013, vol. 441, pp. 15–18.
3. Wang, L., Guo, S.H., Gao, J.Y., Yang, L., Hu, T., Peng, J.H., Hou, M., and Jiang, C.Y., Microwave sintering behavior of FeCuCo based metallic powder for diamond alloy tool bit, *J. Alloys Compd.*, 2017, vol. 727, pp. 94–99.
4. Wang, J.L. and Zhang, S.H., A new diamond bit for extra-hard, compact and nonabrasive rock formation, *J. Cent. South Univ.*, 2015, vol. 22, no. 4, pp. 1456–1462.
5. Jia, M., Cai, J., Ouyang, Z., Shen, L., Wu, H., and Li, C., Design & application of diamond bit to drilling hard rock in deep borehole, *Procedia Eng.*, 2014, vol. 73, pp. 134–142.
6. Gao, C., Yuan, J.T., Jin, H., and Song, Z.Q., Wear characteristics of impregnated diamond bit in drilling armor ceramic, *Adv. Mater. Res.*, 2011, vols. 179–180, pp. 1150–1155.
7. Piri, M., Hashemolhosseini, H., Mikaeil, R., Ataei, M., and Baghbanan, A., Investigation of wear resistance of drill bits with WC, diamond-DLC, and TiAlSi coatings with respect to mechanical properties of rock, *Int. J. Refract. Met. Hard Mater.*, 2020, vol. 87, 105113.
8. Tan, S.C., Li, C.P., Fang, X.H., Shi, H.C., Duan, L.C., and Li, C.L., Investigation of filling phase percentages on the performance of WC-Cu based hot-pressing diamond bit matrices, *Metals*, 2019, vol. 9, no. 12, 1305.
9. Yang, K.H., Pan, B.S., and Duan, L.C., Study on diamond bit for hard and compact rock, *Key Eng. Mater.*, 2004, vols. 259–260, pp. 46–49.
10. Li, C.L., Duan, L.C., Tan, S.C., Zhang, W.J., and Pan, B.S., Effect of CaF<sub>2</sub> and hBN on the mechanical and tribological properties of Fe-based impregnated diamond bit matrix, *Int. J. Refract. Met. Hard Mater.*, 2018, vol. 75, pp. 118–125.
11. Xie, L.L., Chen, L.Y., and Huang, X.L., Effect of graphite addition on impregnated diamond bit properties, *J. Superhard Mater.*, 2019, vol. 41, no. 4, pp. 237–246.
12. Bondarenko, N.A., Novikov, N.V., Mechanik, V.A., Olejnik, G.S., and Vereshchaka, V.M., Structural peculiarities of highly wear-resistant superhard composites of the diamond–WC–6Co carbide system, *Sverkhtverd. Mater.*, 2004, no. 6, pp. 3–15.
13. Novikov, N.V., Bondarenko, N.A., Zhukovskii, A.N., and Mechanik, V.A., The effect of diffusion and chemical reactions on the structure and properties of drill bit inserts. 1. Kinetic description of systems C<sub>diamond</sub>–VK<sub>6</sub> and C<sub>diamond</sub>–(VK<sub>6</sub>–CrB<sub>2</sub>–W<sub>2</sub>B<sub>5</sub>), *Fiz. Mezomekh.*, 2005, vol. 8, no. 2, pp. 99–106.
14. Bondarenko, N.A., Zhukovsky, A.N., and Mechanik, V.A., Analysis of the basic theories of sintering of materials. 1: Sintering under isothermal and nonisothermal conditions (A review), *Sverkhtverd. Mater.*, 2006, no. 6, pp. 3–17.
15. Kolodniits'kyi, V.M. and Bagirov, O.E., On the structure formation of diamond containing composites used in drilling and stone working tools (A review), *J. Superhard Mater.*, 2017, vol. 39, no. 1, pp. 1–17.
16. Bondarenko, M.O., Mechanik, V.A., and Suprun, M.V., Shrinkage and shrinkage rate behavior in C<sub>diamond</sub>–Fe–Cu–Ni–Sn–CrB<sub>2</sub> system during hot pressing of pressureless-sintered compacts, *J. Superhard Mater.*, 2009, vol. 31, no. 4, pp. 232–240.
17. Mechnyk, V.A., Diamond–Fe–Cu–Ni–Sn composite materials with predictable stable characteristics, *Mater. Sci.*, 2013, vol. 48, no. 5, pp. 591–600.
18. Mechanik, V.A., Production of diamond–(Fe–Cu–Ni–Sn) composites with high wear resistance, *Powder Metall. Met. Ceram.*, 2014, vol. 52, nos. 9–10, pp. 577–587.

19. Gevorkyan, E., Mechnik, V., Bondarenko, N., Vovk, R., Lytovchenko, S., Chishkala, V., and Melnik, O., Peculiarities of obtaining diamond–(Fe–Cu–Ni–Sn) composite materials by hot pressing, *Funct. Mater.*, 2017, no. 24, pp. 31–45.
20. Mechnik, V.A., Bondarenko, N.A., Kuzin, N.O., and Gevorkian, E.S., Influence of the addition of vanadium nitride on the structure and specifications of a diamond–(Fe–Cu–Ni–Sn) composite system, *J. Frict. Wear*, 2018, vol. 39, no. 2, pp. 108–113.
21. Mechnik, V.A., Bondarenko, N.A., Kuzin, N.O., and Lyashenko, B.A., The role of structure formation in forming the physicomechanical properties of composites of the diamond–(Fe–Cu–Ni–Sn) system, *J. Frict. Wear*, 2016, vol. 37, no. 4, pp. 377–384.
22. Mechnyk, V.A., Regularities of structure formation in diamond–Fe–Cu–Ni–Sn–CrB<sub>2</sub> systems, *Mater. Sci.*, 2013, vol. 49, no. 1, pp. 93–101.
23. Mechnik, V.A., Effect of hot recompaction parameters on the structure and properties of diamond–(Fe–Cu–Ni–Sn–CrB<sub>2</sub>) composites, *Powder Metall. Met. Ceram.*, 2014, vol. 52, nos. 11–12, pp. 709–721.
24. Mechnik, V.A., Bondarenko, N.A., Dub, S.N., Kolodnitskyi, V.M., Nesterenko, Yu.V., Kuzin, N.O., Zakiev, I.M., and Gevorkyan, E.S., A study of microstructure of Fe–Cu–Ni–Sn and Fe–Cu–Ni–Sn–VN metal matrix for diamond containing composites, *Mater. Charact.*, 2018, vol. 146, pp. 209–216.
25. Mechnik, V.A., Bondarenko, N.A., Kolodnitskyi, V.M., Zakiev, V.I., Zakiev, I.M., Storchak, M., Dub, S.N., and Kuzin, N.O., Physico-mechanical and tribological properties of Fe–Cu–Ni–Sn and Fe–Cu–Ni–Sn–VN nanocomposites obtained by powder metallurgy methods, *Tribol. Ind.*, 2019, vol. 41, no. 2, pp. 188–198.
26. Mechnik, V.A., Bondarenko, N.A., Kolodnitskyi, V.M., Zakiev, V.I., Zakiev, I.M., Ignatovich, S.R., Dub, S.N., and Kuzin, N.O., Formation of Fe–Cu–Ni–Sn–VN nanocrystalline matrix by vacuum hot pressing for diamond-containing composite: Mechanical and tribological properties, *J. Superhard Mater.*, 2019, vol. 41, no. 6, pp. 388–401.
27. Mechnik, V.A., Bondarenko, N.A., Kolodnitskyi, V.M., Zakiev, V.I., Zakiev, I.M., Ignatovich, S.R., Dub, S.N., and Kuzin, N.O., Effect of vacuum hot pressing temperature on the mechanical and tribological properties of the Fe–Cu–Ni–Sn–VN composites, *Powder Metall. Met. Ceram.*, 2020, vol. 58, nos. 11–12, pp. 679–691.
28. Aleksandrov, V.A., Akekseenko, N.A., and Mechnik, V.A., Study of force and energy parameters in cutting granite with diamond disc saws, *Sov. J. Superhard Mater.*, 1984, vol. 6, no. 6, pp. 46–52.
29. Zhukovskii, A.N., Maistrenko, A.L., Mechnik, V.A., and Bondarenko, N.A., The stress-strain state of the bonding around the diamond grain exposed to normal and tangent loading components. Part 1: Model, *Trenie Iznos*, 2002, vol. 23, no. 2, pp. 146–153.
30. Zhukovskii, A.N., Maistrenko, A.L., Mechnik, V.A., and Bondarenko, N.A., Stress-strain state of the matrix around the diamond grain exposed to the normal and tangent loading components. Part 2: Analysis, *Trenie Iznos*, 2002, vol. 23, no. 4, pp. 393–396.
31. Aleksandrov, V.A., Zhukovskii, A.N., and Mechnik, V.A., Temperature field and wear of heterogeneous diamond wheel under conditions of convectional heat transfer. Part 2, *Trenie Iznos*, 1994, vol. 15, no. 2, pp. 196–201.
32. Dutka, V.A., Kolodnitskii, V.M., Zabolotnyi, S.D., Sveshnikov, I.A., and Lukash, V.A., Simulation of the temperature level in rock destruction elements of drilling bits, *Sverkhverd. Mater.*, 2004, no. 2, pp. 66–73.
33. Dutka, V.A., Kolodnitskii, V.M., Mel'nicuk, O.V., and Zabolotnyi, S.D. Mathematical model for thermal processes occurring in the interaction between rock destruction elements of drilling bits and rock mass, *Sverkhverd. Mater.*, 2005, no. 1, pp. 67–77.
34. Sveshnikov, I.A. and Kolodnitskii, V.N., Optimization of the hard alloy cutter arrangement in the drilling bit body, *Sverkhverd. Mater.*, 2006, vol. 28, no. 4, pp. 70–75.
35. de Oliveira, L.J., Cabral, S.C., and Filgueira, M., Study hot pressed Fe-diamond composites graphitization, *Int. J. Refract. Met. Hard Mater.*, 2012, vol. 35, pp. 228–234.
36. Efremenko, V.G., Shimizu, K., Noguchi, T., Efremenko, A.V., and Chabak, Yu.G., Impact–abrasive–corrosion wear of Fe-based alloys: Influence of microstructure and chemical composition upon wear resistance, *Wear*, 2013, vol. 305, nos. 1–2, pp. 155–165.
37. Loginov, P.A., Zhassay, U.A., Bychkov, M.Y., Petrzik, M.I., Mukanov, S.K., Sidorenko, D.A., Orekhov, A.S., Rupasov, S.I., and Levashov, E.A., Chromium-doped Fe–Co–Ni binders for diamond cutting tools: The features of the structure, mechanical properties, and adhesion to diamond, *Int. J. Refract. Met. Hard Mater.*, 2020, vol. 92, 105289.
38. Wu, Y.P., Yan, Q.Z., and Zhang, X.X., Wear characteristics of Fe-based diamond composites with cerium oxide (CeO<sub>2</sub>) reinforcements, *Int. J. Refract. Met. Hard Mater.*, 2020, vol. 86, 105093.
39. Wang, F.L., Kimio, W., Li, Y.P., Ito, S., Yamanaka, K., Koizumi, Y., and Chiba, A., Study of microstructure evolution and properties of Cu–Fe microcomposites produced by a pre-alloyed powder method, *Mater. Des.*, 2017, vol. 126, pp. 64–72.
40. Zhao, C., Wang, Z., Li, D.X., Xie, M.S., Kollo, L., Luo, Z.Q., Zhang, W.W., and Prashanth, K.G., Comparison of additively manufacturing samples fabricated from pre-alloyed and mechanically mixed powders, *J. Alloys Compd.*, 2020, vol. 830, 154603.

41. Bai, R., Zhang, S.H., Han, Y., Zhou, H., Su, Z., Wang, J.L., Wu, J.J., and Liu, L.L., Effect of CL192 pre-alloyed powder on matrix properties of impregnated diamond bit, *Diamond Relat. Mater.*, 2020, vol. 107, 107878.
42. Xie, D.L., Qin, H.Q., Lin, F., Pan, X.Y.I., Chen, C., Xiao, L.Y., Chen, J.R., and Mo, P.C., Microstructures and properties of Fe–Co–Cu pre-alloyed powder for geological diamond bits, *J. Superhard Mater.*, 2019, vol. 41, no. 5, pp. 302–309.
43. Zhou, J.Z., Liu, X.L., Huang, K.H., Dong, M.S., and Jiang, H.H., Application of the mixture design to design the formulation of pure cultures in Tibetan kefir, *Agric. Sci. China*, 2007, vol. 6, no. 11, pp. 1383–1389.
44. Mahdhi, A., Harbi, B., Esteban, M.Á., Chaieb, K., Kamoun, F., and Bakhrouf, A., Using mixture design to construct consortia of potential probiotic *Bacillus* strains to protect gnotobiotic *Artemia* against pathogenic *Vibrio*, *Biocontrol Sci. Technol.*, 2010, vol. 20, no. 9, pp. 983–996.
45. Kim, S.M., Surimi–alginate gels as affected by setting: A study based on mixture design and regression models, *Food Res. Int.*, 2003, vol. 36, no. 3, pp. 295–302.
46. Shi, C.J., Wu, Z.M., Lv, K.X., and Wu, L.M., A review on mixture design methods for self-compacting concrete, *Constr. Build. Mater.*, 2015, vol. 84, pp. 387–398.
47. Ly, O., Monchau, F., Remond, S., Lors, C., Jouanneaux, A., Debarre, E., and Damidot, D., Optimization of the formulation of an original hydrogel-based bone cement using a mixture design, *J. Mech. Behav. Biomed. Mater.*, 2020, vol. 110, 103886.
48. Achour, S., Khelifi, E., Ayed, L., Helal, A.N., and Bakhrouf, A., Response surface methodology for textile wastewater decolourization and biodegradation by a novel mixed bacterial consortium developed via mixture design, *Desalin. Water Treat.*, 2014, vol. 52, nos. 7–9, pp. 1539–1549.
49. Silvestrini, R.T., Considerations for D-optimal sequential design: Considerations for D-optimal sequential design, *Qual. Reliab. Eng. Int.*, 2015, vol. 31, no. 3, pp. 399–410.
50. El-Malah, Y., Nazzal, S., and Khanfar, N.M., D-optimal mixture design: Optimization of ternary matrix blends for controlled zero-order drug release from oral dosage forms, *Drug Dev. Ind. Pharm.*, 2006, vol. 32, no. 10, pp. 1207–1218.
51. Yin, H.F., Chen, Z.G., Gu, Z.X., and Han, Y.B., Optimization of natural fermentative medium for selenium-enriched yeast by D-optimal mixture design, *LWT–Food Sci. Technol.*, 2009, vol. 42, no. 1, pp. 327–331.
52. Rahul, A.V., Santhanam, M., Meena, H., and Ghani, Z., 3D printable concrete: Mixture design and test methods, *Cem. Concr. Compos.*, 2019, vol. 97, pp. 13–23.

# 自动化泥浆循环净化装置机械系统设计与研制

柴晓然<sup>1,2</sup> 孙武成<sup>3</sup> 段隆臣<sup>3</sup> 董高峰<sup>1,2</sup> 臧丽萍<sup>1,2</sup>

(1. 青海省环境地质重点实验室, 青海 西宁 810000; 2. 青海省地质环境保护与灾害防治工程技术研究中心, 青海 西宁 810000; 3. 中国地质大学(武汉)工程学院, 湖北 武汉 430074)

**摘要** 针对水文地质钻探现场中通过人工捞砂处理泥浆的低质低效问题,石油等领域结构复杂、体积庞大、功耗巨大的固控设备无法直接移植借鉴,现今大多数解决方案仅仅是在泥水分离方法上从开挖沉淀池过渡到使用筛分机械,尽管能够提高泥浆净化效率,但仍无法克服占地面积大并伴随严重污染的局限性。为此,设计了一种组合配浆、混浆和泥浆净化的泥浆处理装置机械系统。结合沉淀法与机械分离法,将箱体与振动筛组合为一体,通过管道实现泥浆不落地的输运存储和筛分净化;联接泥浆泵、振动筛、搅拌器等工作部件线路并接入PLC,通过控制面板进行远端的自动及半自动控制;优化部件装配结构,达到拆装方便、车载运移的目的。针对青海省高海拔、极端气温等复杂地质与气候环境下工作泵压较正常情况偏低、工作介质结冰等问题,调节电路部件功率并增设温度调节设备,同时结合地质勘察领域对绿色勘查的环保要求,研制了一种自动化泥浆净化循环装置。经过现场试验验证,该装置能够在手动或自动模式下平稳高效地完成泥浆净化循环工作,运行过程中泥浆分散均匀且性质稳定,在现场工作规程下处理量可达60 m<sup>3</sup>/h,不含电加热总功率小于32 kW。该型装置适合于工程地质勘察钻探、水文地质及水井钻探等较小规模施工应用。

**关键词** 绿色勘查 泥浆净化 自动控制 机械系统

中图分类号 TD12,P642

文献标志码 A

文章编号 1001-1250(2019)-07-182-07

DOI 10.19614/j.cnki.jsks.201907030

## Design and Development of Mechanical System for an Automatic Mud Circulation and Purification Device

Chai Xiaoran<sup>1,2</sup> Sun Wucheng<sup>3</sup> Duan Longchen<sup>3</sup> Dong Gaofeng<sup>1,2</sup> Zang Liping<sup>1,2</sup>

(1. Qinghai Key Laboratory of Environmental Geology, Xining 810000, China; 2. Engineering and Technology Research Center of Geological Environmental Protection and Disaster Prevention in Qinghai Province, Xining 810000, China; 3. Faculty of Engineering, China University of Geosciences, Wuhan 430074, China)

**Abstract** In view with of the low quality and inefficiency of slurry treatment by artificial salvage in hydrogeological drilling, solids control equipment with complex structure, huge volume and extreme power consumption in oil field can not be directly transplanted for reference. Nowadays, most of the solutions are just moving from excavating sedimentation tank to making use of vibrating screen. Although there is a significant improvement of efficiency in slurry purification by this way, they still can not get rid of the shortcomings of occupying large area and causing severe pollution. In order to solve the above existing problems, a mechanical system of slurry treatment equipment is designed, which combines slurry making, mixing and purification. Combining two purification theory, i.e., sedimentation and mechanical separation, the box body and vibration screen are assembled, making slurry transported, stored and screened through pipes; connecting the circuits of working parts like slurry pump, vibration screen, agitator and collecting them to PLC, remote automatic and semi-automatic control can be realized with control panel; optimizing the assembly structure of all components to achieve shortcut disassembly and assembly, loading and transportation. Aiming at the problems of low working pump pressure and icing of working medium in complex geological and climatic environments such as high altitude and extreme temperature in Qinghai Province, according to the requirements for environmental protection of green exploration in geological prospecting, an automatic mud circulation and purification device has been developed by adjusting the power of circuit components and adding temperature regulating equipment. The field test

收稿日期 2019-04-30

基金项目 青海省科技计划项目(编号:2017-ZJ-Y25),中国地质大学(武汉)研究项目(编号:2018058028)。

作者简介 柴晓然(1969—),男,工程师。通讯作者 段隆臣(1967—),男,教授,博士,博士研究生导师。

result show that the device can complete the mud purification cycle smoothly and efficiently in manual or automatic mode, the mud can be uniformly dispersed and stable in operation even while the processing capacity reach  $60 \text{ m}^3/\text{h}$  under the field operating rules, and the total power of electric heating is below 32 kW without considering heating consumption. The study results further indicated that the device developed in this paper is suitable for the light and simple application of small scale construction such as engineering geological exploration, hydrogeology and water well drilling.

**Keywords** Green exploration, Mud purification, Automatic control, Mechanical system

青海作为西藏、新疆地区联接内地的纽带,资源总量非常丰富,种类较为齐全。但由于其地处青藏高原,生态系统极为脆弱,传统的矿产开发方式会对植被、水资源等生态环境造成严重破坏<sup>[1-2]</sup>。当地地质勘探和水文钻井钻探现场的施工条件比较简陋,其泥浆循环净化方式大多为粗放式的人工挖槽、捞砂,不仅施工过程耗时耗力,而且泥浆净化效率和效果不理想,亟待探索一种符合绿色勘查规范并能有效满足青海省地勘需求的新型泥浆处理方案。

现阶段,绿色发展已成为矿业健康持续发展的时代要求<sup>[3]</sup>,绿色勘查则是绿色发展理念在地质勘查领域的具体实践<sup>[4]</sup>,通过在勘察工作中减小对生态环境的扰动,实现生态保护和资源供给的双赢<sup>[5-7]</sup>。2018年下半年,第一个绿色勘查团体标准——《绿色勘查指南》发布并实施。该标准基于绿色发展、创新驱动、和谐共赢、管理规范的基本原则,在勘察设计、勘察实施的基本要求下,对场地建设、现场管理、水和野生动植物保护、噪声粉尘与废弃物管理、环境恢复治理、智能化和科技创新等做出了具体规范和指导。

现场钻探施工中,对钻探施工设备及配套技术水平、钻探施工工艺设计和选择、钻探施工循环液环保标准具有较高要求。泥浆固控装置广泛应用于非开挖钻进<sup>[8]</sup>、地质岩芯钻探<sup>[9]</sup>、桩基工程<sup>[10-11]</sup>、盾构施工<sup>[12]</sup>、废液处理<sup>[13]</sup>等领域,在结构特点上,也有各式模块化<sup>[14-15]</sup>、自动化<sup>[16-17]</sup>、可移动<sup>[18-19]</sup>固控系统,尤其在石油钻井中应用广泛<sup>[20]</sup>,已实现系列化、标准化和专用化。由于施工环境、领域不同,钻进深度、口径和工艺等方面的巨大差异,将直接导致设备结构组合、工作参数不匹配,尤其是过大的体积、过高的功耗无法满足绿色勘查对于设备小型化的需求。

本研究参照施工设备应具备安、拆快捷,便于搬运,机械化、智能化程度高,施工操作安全简便、劳动强度低、生产效率高,工程质量好、节能、环保等要求,结合青海省地质、气候环境和现场施工技术条件,对模块化、轻便化、小型化、集成度高的泥浆净化设备进行设计和研制,主要对该型装置的组合结构、部件选配等进行设计,并通过现场试验考察整个装置的可靠性。

## 1 装置组成结构与工作原理

自动化泥浆循环净化装置结构如图1所示。

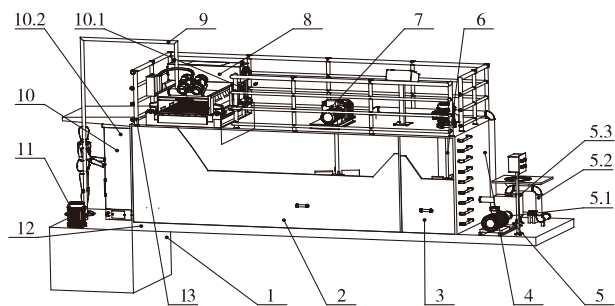


图1 自动化泥浆循环净化装置结构

Fig. 1 Structural of automatic mud circulation and purification device

1—地埋罐; 2—净化仓; 3—配浆仓; 4—清水仓; 5—混浆装置;  
5.1—砂泵; 5.2—喷射混合漏斗用管汇; 5.3—阀门组; 6—配浆仓搅拌器;  
7—净化仓搅拌器; 8—高效振动筛; 9—抽吸管道; 10—电气控制系统;  
10.1—近端控制子系统; 10.2—远端集成控制子系统;  
11—渣浆泵; 12—撬装板; 13—护栏

装置中,地埋管及净化仓、配浆仓、清水仓3个泥浆仓作为储浆部件用于储存泥浆,确保泥浆在管路通道中循环流动。该装置的泥浆循环净化方式为:  
①混浆装置5中砂泵通过管汇、阀门组组合泵送配浆材料与清水仓4中由外部抽吸来的清水进行混合预配泥浆,并汇入配浆仓3中;②新配泥浆被抽吸至钻机中帮助钻进,钻机作业的同时井口将持续上返泥浆;③上返泥浆被导流至地埋罐1中进行大颗粒沉淀后,被渣浆泵11抽吸至振动筛8上进行筛除净化;④经筛除净化后的泥浆向下汇入净化仓2中;⑤因净化仓2与配浆仓3上部连通,净化仓2中的筛后泥浆与配浆仓3中的新配泥浆将一并被抽吸至钻机中继续参与循环以帮助钻进。

净化仓、配浆仓2个储浆仓均在正上方开口区域装载搅拌器,实现对新配泥浆及筛除净化泥浆的均匀度控制,保障泥浆性能的稳定性;净化仓部分底部安装有加热装置,防止在高寒地区泥浆被冻住,可满足系统在高寒地区水文地质井泥浆净化需要;在电气控制系统中,泥浆泵、振动筛、混浆装置等部件通过自留开关实现近端开闭控制,集成线路于控制柜中通过接线箱的控制面板完成远端控制。

## 2 装置设计特点

根据施工现场环境和工程需要,自动化泥浆循

环净化装置设计适用最大井深300 m,最大钻井口径750 mm,最大成井口径325 mm。

通过地理罐和振动筛对利用沉淀池、机械分离进行泥水处理的2种常用方法进行整合,该装置能较好地平衡施工场地规模限制和设备维护成本的要求,达到提高处理效率、降低施工成本的目的。

该装置电气控制系统由容纳电源、断路器、继电器、PLC(可编程控制器)等电气装置的控制柜和装载控制面板的60 A一进八出集线箱组成。通过各个工作装置的线路连接,实现对渣浆泵、振动筛、砂泵、加热装置和2个搅拌器等部件的近端直接开关和远端联调控制。为满足现场恶劣的环境条件,电气控制系统控制柜采用防爆、防水、防尘控制柜。根据现场环境条件,选择相应的防爆防水防尘等级,防护等级 $\geq IP54$ 。控制系统核心选择美国AB公司生产的PLC,具有一定的温度适应范围,防尘,防水,防爆等级 $\geq IP21$ 。同时控制柜内置自动温度调节装置,确保柜内器件在适宜的温度下正常运行。

装置电气控制系统中,设计远端联调控制分为手动、自动2种模式。手动模式下,依靠控制面板上的按钮开关影响控制柜内继电器的开闭,进行相关部件的开关控制;自动模式下,需要在地理罐、净化仓、配浆仓、清水仓中加装行程开关,将其液位达到上下限位而产生的开关信号输入PLC,利用既定逻辑程序由PLC产生输出信号控制继电器开闭。远端控制的控制面板如图2所示。



图2 远端控制面板

Fig. 2 Remote control panel

为实现自动化泥浆循环净化装置的轻便化移动需求,达到拆装、运输方便的效果,采用可拆卸化设计思路。通过运输装置的吊装设备进行起吊装车和吊卸安装,节省装置安装、拆卸的人力负担,节约占地面积和施工成本。其中,运载装置使用具有越野能力和环境适应性的卡车,并对卡车后部进行改造,添加泥浆循环净化仓底部撬装面配套的安装面。

工作时,运载装置与泥浆循环净化仓分离,可单独作为钻探现场的运载车辆使用;运输时,将地理罐、振动筛、渣浆泵、抽吸管道等拆卸,泥浆仓与运载

装置通过螺栓固连,其中护栏与仓体采用螺栓连接,可拆卸,在运输状态时卸下以满足公路运输的限高要求。装置的2种使用状态如图3所示。

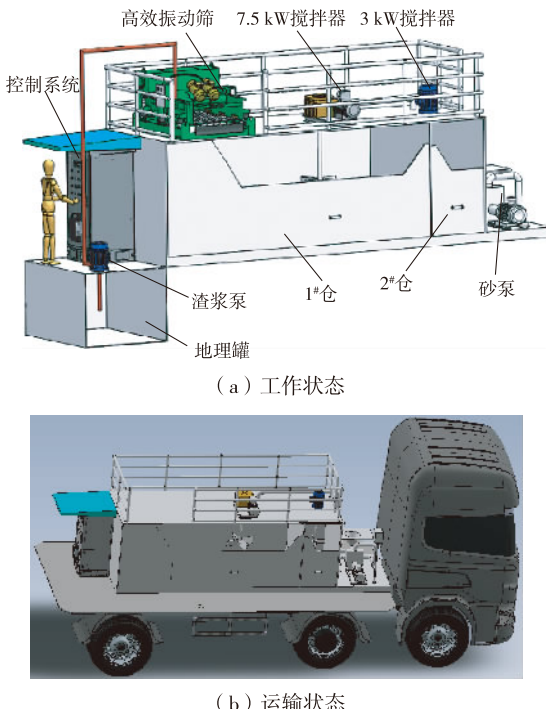


图3 自动化泥浆循环净化装置的使用状态

Fig. 3 Application state of the automatic mud circulation and purification device

### 3 关键组成部分选型与设计

#### 3.1 储浆部件选型设计

根据总体设计方案中的成井口径等参数,可以计算出固控系统的泥浆储备量,进而确定各储浆部件所需容积。

(1)每米泥浆用量。计算公式为

$$Q_{\text{每米用量}} = V_{\text{钻孔体积}} \cdot d_{\text{孔径系数}}, \quad (1)$$

以最大成孔口径750 mm计算,得到泥浆每米用量为0.52 m<sup>3</sup>。

(2)每台班泥浆用量。计算公式为

$$Q_{\text{每台班用量}} = 10Q_{\text{每米用量}}, \quad (2)$$

按生产经验(即每工作台班纯进尺10 m)计算,可得泥浆每台班用量为5.2 m<sup>3</sup>。

(3)每台班最小泥浆储备量。根据相关经验,考虑地层漏失、泥浆泵流量等因素,每台班实际储备量一般为每台班用量的2.5~3倍,据此计算每台班最小储备量:

$$Q_{\text{每台班最小储量}} = 3Q_{\text{每台班用量}}, \quad (3)$$

即得每台班的泥浆储备量至少为15.6 m<sup>3</sup>。同时考虑泥浆的地层滤失和管汇泄露,结合占地面积要求,本研究设计的泥浆仓总容积为16.5 m<sup>3</sup>,地理罐容积为3 m<sup>3</sup>。储浆部件选型参数如表1所示。

**表1 自动化泥浆循环净化装置储浆部件选型参数****Table 1 Selection parameter of the slurry storage components of automatic mud circulation and purification device**

储浆部件	容积 /m <sup>3</sup>	外形尺寸/m			钢材厚度/mm		质量 /kg	
		长度	宽度	高度	侧板	底板		
地理罐	3.0	2 000	1 500	1 200	4	5	1 030	
净化仓	10.5	5 900	2 000	2 030	5	6	3 000	
泥浆仓	配浆仓	3.0	5 900	2 000	2 030	6	6	3 000
清水仓	3.0	5 900	2 000	2 030	6	6	3 000	

### 3.2 泥浆泵选型设计

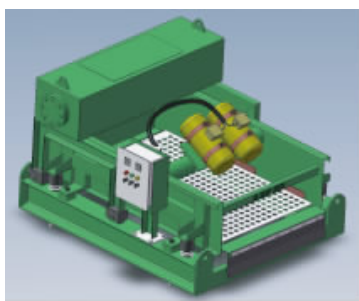
青海施工现场往期钻进需求的最大泵量为60 m<sup>3</sup>/h,本研究设计的渣浆泵和砂泵的最大处理量均为70 m<sup>3</sup>/h,满足单一泥浆泵工作需要。根据现场供电情况与泵浆能力需求,一般选择2台电机功率均为7.5 kW的泥浆泵,但为适应青海高海拔地区水文地质井渣浆抽吸需求,渣浆泵功率在原功率基础上增加至11 kW。最终泥浆泵选型参数如表2所示。

**表2 自动化泥浆循环净化装置泥浆泵技术参数****Table 2 Technical parameters of mud pump of automatic mud circulation and purification device**

泥浆泵	外形尺寸/m			电机 功率/kW	最大处理 量/(m <sup>3</sup> /h)
	长度	宽度	高度		
渣浆泵	1 650	700	400	11.0	70
砂泵	1 850	800	750	7.5	70

### 3.3 振动筛选型设计

本研究设计的自动化泥浆循环净化装置选用一种高效振动筛,外观如图4所示。

**图4 振动筛****Fig. 4 Vibrating screen**

该型振动筛设计的最大处理量与泥浆泵的最大处理量保持一致,外形尺寸与泥浆循环净化仓上开口面相匹配,过滤面积根据装置最大处理量设计为1.8 m<sup>2</sup>。具体选型参数如表3所示。

**表3 振动筛技术参数****Table 3 Technical parameter of vibration screen**

处理量 /(m <sup>3</sup> /h)	振动电机 功率/kW	外形尺寸 /mm	筛网规格 /mm	过滤面积 /m <sup>2</sup>	质量 /kg
70	2×1.1	1 950×1 650 ×1 400	2×1 090 ×830	1.8	1 050

对于产生激振力的振动筛振源体,需要降低减

振体(整个装置系统)的振动强度,尤其需要考虑本研究装置设计的振动筛安置于泥浆仓上方,极易产生较大共振和噪声。通常采取的减振措施主要有抑制振源强度、隔振、消振。但对于振动筛这种利用振动进行生产作用的振动机械,减振方式有所不同,即不允许采取措施抑制振源的振动<sup>[21]</sup>。

在本装置中,通过在振动筛与下部泥浆仓的连接处添加柔软衬垫,依靠其变形减轻振源对减振体的激励进行隔振;对于3个泥浆仓,主要通过整体部件设计使装置质量分布平衡,同时通过减小迎风面面积,从而减轻其承受的风载并抑制共振;对于装置整体,通过在装置底座下方添加木块基础进行隔振。同时,为对控制柜中的电气装置进行有效防护,在控制柜底部加厚防震垫并在关键部位填充泡沫进行缓冲消振。

### 3.4 搅拌器选型设计

按实际工作需要设计的搅拌器技术参数如表4所示。

**表4 搅拌器技术参数****Table 4 Technical parameters of mixer**

搅拌器	外形尺寸/m			质量 /kg	电机 功率/kW	叶轮 转速/rpm	叶轮 直径/mm
	长度	宽度	高度				
净化仓中	850	500	450	280	7.5	70	750
配浆仓中	800	400	400	130	3.0	85	400

由于净化仓储存渣浆经过净化处理后的泥浆,故相较于配浆仓,使用的搅拌器需更大型号。两搅拌器均通过法兰面安置于泥浆仓正上方,搅拌器的电机主轴通过钢性联轴器与连接轴垂向固连,叶轮探入仓内泥浆中对泥浆进行搅拌混合。

### 4 现场试验

本研究设计及研制的自动化泥浆循环净化装置在组装调试完成后,通过室内清水泥浆循环测试,对装置运行的稳定性进行了初步验证,室内试验如图5所示。

**图5 室内试验****Fig. 5 Laboratory test**

现场试验的施工目标确定为50 m深的水文地质井,作为当地预建工厂吃水井。泥浆净化现场试验包括泥浆循环净化装置的部件功能验证及泥浆筛除

净化效果测试两方面内容。主要是根据不同深度孔口上返的泥浆和振动筛筛后的泥浆性能差异,即经

过固相控制前后的泥浆含砂量的对比分析,对装置的净化效果进行评价。现场试验如图6所示。



(b) 运输状态

(c) 筛除泥浆废渣

图 6 现场试验

Fig. 6 Field test

经过现场试验,证明本研究装置的各部件功能符合预期,即泥浆存储、循环状态平衡稳定,渣浆抽吸符合既定功率需求,新配泥浆分散均匀且性质优

异,泥浆加热状态稳定效果优良,泥浆仓储液面平稳且液位能够控制在合理区间。自动化泥浆净化循环装置的运行流程如图7所示。

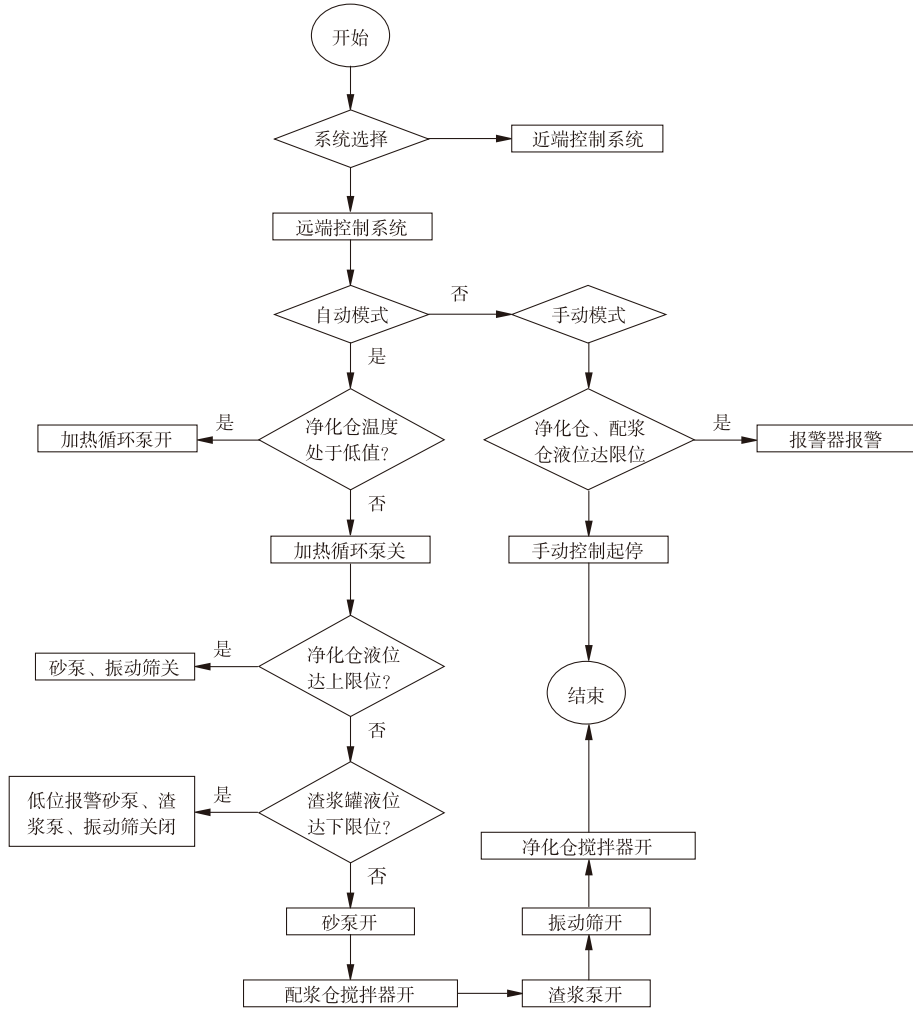


图 7 自动化泥浆净化循环装置运行流程

Fig. 7 Running process of automatic mud circulation and purification device

为有效评价装置的净化效果,以钻进深度进行划分,除去实际钻进中受操作进程影响的数据,得到泥浆固相控制前后的含砂量如表5所示。

由表5可知:本研究设计的自动化泥浆循环净化

装置对于泥浆净化效果明显,含砂量的平均优化率达到23.68%。参考同类钻井液振动筛的工业性试验结果<sup>[22-23]</sup>,钻井液中含砂量降低了20%~30%,说明该装置的处理能力和泥水分离效果能够满足水文地质

**表5 泥浆固相控制前后含砂量对比****Table 5 Contrast of sand content of mud before and after solid phase control**

深度/m	泥浆含砂量/%	
	固相控制前	固相控制后
4	14.5	12.5
6	1.2	1.0
20	4.5	4.0
22	7.0	4.2
30	10.0	6.3

钻井的工作需求。

## 5 结论

(1) 自动化泥浆循环净化装置采用了模块化、轻便化、小型化、集成度高的一体化设计思路,减小了占地面积,实现了在储浆部件与管汇中循环的泥浆不落地工作,起吊装卸方便,大幅度缩短了辅助钻进时间,提高了施工效率。

(2) 通过PLC实现了装置的自动控制,能够自动控制工作装置开关,可实现平稳高效的可控钻进,在节省人力资源的同时,降低施工事故风险。

(3) 该装置在确保各部件正常工作完成预设泥浆循环工作的情况下,能够取得非常优异的泥浆净化效果和地层钻进效率,完全可以取代传统的粗放式泥浆人工净化作业方式。

(4) 尽管该装置能够满足绿色勘查设计要求,但仍有不少改进空间。如装置的一体集成化可进行进一步优化,地埋罐可进行优化设计以整合到主体装置上,进一步缩小占地空间;振动筛筛除泥浆后的废渣处理为后续工序,可以通过添加回收装置加以改善;智能化程度仍有提升空间,未来可通过升级通信技术,来进行远程钻进作业控制和施工风险管控。

## 参 考 文 献

- [1] 徐红燕,陈建平,孔锐,等.青海省绿色矿业发展策略研究[J].国土资源科技管理,2015,32(6):32-39.  
Xu Hongyan, Chen Jianping, Kong Rui, et al. Research on development strategies of green mining in Qinghai Province [J]. Scientific and Technological Management of Land and Resources, 2015, 32 (6):32-39.
- [2] 陈伯辉,高元宏,李玉胜,等.青海省绿色地勘技术及标准探讨[J].探矿工程:岩土钻掘工程,2016,43(10):131-134.  
Chen Baihui, Gao Yuanhong, Li Yusheng, et al. Discussion on the green geological prospecting technique of Qinghai Province and the standard [J]. Exploration Engineering: Rock & Soil Drilling and Tunneling, 2016, 43(10):131-134.
- [3] 鞠建华,强海洋.中国矿业绿色发展的趋势和方向[J].中国矿业,2017,26(2):7-12.  
Ju Jianhua, Qiang Haiyang. The trend and direction of green development of the mining industry in China [J]. China Mining Magazine, 2017, 26(2):7-12.

opment of the mining industry in China [J]. China Mining Magazine, 2017, 26(2):7-12.

- [4] 张新虎,刘建宏,黄万堂,等.绿色勘查理念:认知、探索与实践[J].甘肃地质,2017,26(1):1-7.  
Zhang Xinhua, Liu Jianhong, Huang Wantang, et al. Green exploration:cognition, explore and practice [J]. Gansu Geology, 2017, 26 (1):1-7.
- [5] 吴金生,李子章,李政昭,等.绿色勘查中减少探矿工程对环境影响的技术方法[J].探矿工程:岩土钻掘工程,2016,43(10):112-116.  
Wu Jinsheng, Li Zizhang, Li Zhengzhao, et al. Technological methods of reducing impact on environment by exploration engineering in green exploration [J]. Exploration Engineering: Rock & Soil Drilling and Tunneling, 2016, 43(10):112-116.
- [6] 贾占宏,高元宏,梁俭,等.绿色地质勘查综合技术应用分析[J].探矿工程:岩土钻掘工程,2017,44(4):1-4.  
Jia Zhanhong, Gao Yuanhong, Liang Jian, et al. Application and analysis on comprehensive technology of green geological prospecting [J]. Exploration Engineering: Rock & Soil Drilling and Tunneling, 2017, 44(4):1-4.
- [7] 刘海声,穆元红,刘鹏,等.绿色勘查技术在青海格尔木铜金山矿区钻探施工的应用分析[J].探矿工程:岩土钻掘工程,2017,44(3):27-30.  
Liu Haisheng, Mu Yuanhong, Liu Peng, et al. Application analysis on green exploration technology in drilling construction in Tongjinshan mining area of Qinghai Province [J]. Exploration Engineering: Rock & Soil Drilling and Tunneling, 2017, 44(3):27-30.
- [8] 刘寿军.非开挖定向钻穿越泥浆净化与回收装置的研制[J].石油机械,2006(1):58-60.  
Liu Shoujun. A mud purification and recovery device used for non-open-cut directional drilling [J]. China Petroleum Machinery, 2006 (1):58-60.
- [9] 张飞,熊虎林,吕方,等.GK-15型地质岩心钻探泥浆固控装置研究应用[J].探矿工程:岩土钻掘工程,2015,42(12):64-68.  
Zhang Fei, Xiong Hulin, Lyu Fang, et al. Study and application on GK-15 mud solid-phase control device for geological core drilling [J]. Exploration Engineering: Rock & Soil Drilling and Tunneling, 2015, 42(12):64-68.
- [10] 楼明浩,汪炎法,孔奥,等.桩基施工泥浆固化处理新技术在某工程中的应用[J].施工技术,2015,44(12):97-100.  
Lou Minghao, Wang Yanfa, Kong Ao, et al. Engineering practice of improved sludge dewatering processing technology for piles construction in a project [J]. Construction Technology, 2015, 44(12): 97-100.
- [11] 龙莉波.泥浆净化装置在钻孔灌注桩施工中的应用[J].建筑施工,2007(6):392-394.  
Long Libo. Application of slurry depuration device to bored cast-in-place pile construction [J]. Building Construction, 2007 (6):392-394.
- [12] 刘敏林,王永贵.泥浆处理技术在地铁盾构施工中的应用[J].南水北调与水利科技,2004(5):50-51.  
Liu Minglin, Wang Yonggui. Mud treating technique in metro shield structure construction [J]. South-to-North Water Transfers and Wa-

- ter Science & Technology, 2004(5):50-51.
- [13] 房 凯,张忠苗,刘兴旺,等.工程废弃泥浆污染及其防治措施研究[J].岩土工程学报,2011(S2):238-241.  
Fang Kai, Zhang Zhongmiao, Liu Xingwang, et al. Pollution of construction waste slurry and prevention measures [J]. Chinese Journal of Geotechnical Engineering, 2011(S2):238-241.
- [14] 冯 定,唐海雄,周 魁,等.模块钻机的现状及发展趋势[J].石油机械,2008(9):143-147.  
Feng Ding, Tang Haixiong, Zhou Kui, et al. The progress and developing trends of modular drilling rig [J]. China Petroleum Machinery, 2008(9):143-147.
- [15] 刘兴财.海洋石油模块钻机钻井液固控系统设计[J].化工管理,2017(7):168.  
Liu Xingcai. Design of drilling fluid solid control system for offshore oil modular drilling rig [J]. Chemical Enterprise Management, 2017 (7):168.
- [16] 鲍泽富,刘江波,王江萍,等.钻井液回收净化再利用系统的设计[J].石油机械,2006(6):46-49.  
Bao Zefu, Liu Jiangbo, Wang Jiangping, et al. Design of a system for drilling fluid recovery, purification and reuse [J]. China Petroleum Machinery, 2006(6):46-49.
- [17] 董怀荣,王 平,蔡文军.一种全自动闭环控制钻井液高速离心机[J].西部探矿工程,2006(4):209-211.  
Dong Huairong, Wang Ping, Cai Wenjun. A fully automatic closed-loop control drilling fluid high-speed centrifuge [J]. West-China Exploration Engineering, 2006(4):209-211.
- [18] 杨志远,冯 定,周 魁,等.轻型可搬迁式海洋模块钻修机固控系统研究[J].石油矿场机械,2009,38(11):65-69.
- Yang Zhiyuan, Feng Ding, Zhou Kui, et al. Study on the solid controlling system of light modular ocean drilling machine [J]. Oil Field Equipment, 2009, 38(11):65-69.
- [19] 许锦华,胡小刚,牟长清,等.新型钻机固控系统[J].石油机械,2010(3):34-37.  
Xu Jinghua, Hu Xiaogang, Mou Cangqing, et al. New solid control systems [J]. China Petroleum Machinery, 2010(3):34-37.
- [20] 董怀荣,李宗清,李 琴,等.钻井液固控系统技术现状与发展趋势[J].西部探矿工程,2015(11):49-52.  
Dong Huairong, Li Zongqing, Li Qing, et al. The progress and developing trends of drilling fluid solid control system technology [J]. West-China Exploration Engineering, 2015(11):49-52.
- [21] 刘 杰,孙光复.反共振振动机械的理论及应用[J].东北大学学报:自然科学版,1995(1):82-86.  
Liu Jie, Sun Guangfu. Theory of antiresonant vibrating machine with application [J]. Journal of Northeastern University:Natural Science, 1995(1):82-86.
- [22] 白文雄,李红才,方建国.GW-1双轴平动椭圆钻井液振动筛的研制[J].石油机械,2001(8):17-19.  
Bai Wenxiong, Li Hongcai, Fang Jianguo. Development of double-shaft planar-moving elliptical shape shaker [J]. China Petroleum Machinery, 2001(8):17-19.
- [23] 胡欣峰,侯勇俊,张明洪.平动椭圆钻井振动筛研究的新进展[J].石油机械,2004(12):53-55.  
Hu Xinfeng, Hou Yongjun, Zhang Minghong. New progress in double-shaft planar-moving elliptical shape shaker [J]. China Petroleum Machinery, 2004(12):53-55.

(责任编辑 王小兵)